

Weak Lensing analysis of Abell 2390 using short exposures

A.DUTTA ¹, J.R.PETERSON,¹ T. ROSE,² M. CIANFAGLIONE,³ A. BONAFEDE,³ G. LI,⁴ AND G. SEMBROSKI¹

¹*Department of Physics and Astronomy
Purdue University*

West Lafayette, Indiana, USA

²*Waterloo Center for Astrophysics*

University of Waterloo

Waterloo, Ontario, Canada

³*Department of Physics and Astronomy
University of Bologna*

Bologna, Italy

⁴*Purple Mountain Observatory*

West Beijing Road, Nanjing 210008

People's Republic of China

ABSTRACT

We present a weak lensing analysis of the galaxy cluster Abell 2390 at $z = 0.23$ using second moment shape measurements made in 411 short 60s exposures. The exposures are obtained in three broadband photometric filters (g, r, i) using WIYN-ODI. Shape measurement in individual exposures is done using a moment matching algorithm. Forced measurement is used when the moment matching algorithm fails to converge at low signal to noise ratio (SNR). The measurements made in individual images are combined using inverse error weight to obtain accurate shape of sources and hence recover shear. We use PhoSim simulations to validate shear measurements recovered by our pipeline. We find the mass of Abell 2390 is in agreement with previously published results. We also find the E-Mode maps show filamentary structures consistent with baryonic structures and recovers most clusters/groups of galaxies found using Optical and X-Ray data. Thus we demonstrate the feasibility of using Weak Lensing to map large scale structure of the universe. We also find the central portion of the cluster has a bimodal mass distribution and the relative orientation of the peaks are similar to X-Ray. We discuss earlier research on this galaxy cluster and show that a late stage merger accounts for all the observed data.

Keywords: Weak lensing, Galaxy Clusters

1. INTRODUCTION

Galaxy clusters are the largest bound structures in the Universe containing a few hundred to a few thousand individual galaxies. They play an important role in our understanding of the Universe and hierarchical structure formation (Press & Schechter 1974; Bond et al. 1991; Lacey & Cole 1993; Kravtsov & Borgani 2012). Mass profiles of galaxy clusters are fundamental to understanding structure formation and constraining cosmological models (Holder et al. 2001; Cunha et al. 2009). However, the measurement of this is made challenging by the fact that only about 5% of the total mass of galaxy clusters emits light in the visible spectrum. About 15% of the mass emits light in the form of ionized X-Rays and the remaining 80% is expected to be in the form of dark matter (Fukugita et al. 1998).

Different methods of measuring masses of galaxy clusters exist. X-Ray observations of hot ionized ICM are expected to trace the general mass profile of a cluster. This method has been widely used along with assumptions of hydrostatic

equilibrium and/or a mass profile such as NFW (Navarro et al. 1995; Evrard et al. 1996; Reiprich & Böhringer 2002; Ettori et al. 2013) to measure the mass of galaxy clusters. These assumptions limit our ability to make accurate measurements since clusters are always in a dynamical state (Piffaretti & Valdarnini 2008). These include cooling flows and AGN feedback (Fabian 1994; Gitti et al. 2012), mergers with other clusters and smaller infalling groups. This is expected since clusters lie at the major intersections of the filamentary structure of the Universe (van Haarlem & van de Weygaert 1993). Another method of measuring cluster masses is with the velocity dispersion of the cluster members along with the assumption of virial equilibrium (Zwicky 1933, 1937; Smith 1936; Danese et al. 1980). However, a significant majority of the clusters are in a dynamical state where the assumption of virial equilibrium might not hold. The Sunyaev–Zeldovich effect (Sunyaev & Zeldovich 1972, 1970, 1980; Carlstrom et al. 2002) has also been used to measure the mass of galaxy clusters. However, this approach is limited by the high quality of data required, mass-observable scaling relation, and dynamical state of the cluster (Krause et al. 2011; Dietrich et al. 2018).

Weak lensing provides another independent method to measure mass. In weak lensing, coherent distortions in background galaxies (Tyson et al. 1990; Kaiser et al. 1995; Squires et al. 1996) are used to infer mass. Unlike other methods, weak lensing makes no assumption about the state of the cluster and directly probes mass. It is equally sensitive to both baryonic matter and dark matter (DM), making it an ideal tool to directly probe DM distribution in the Universe. Several excellent weak lensing studies on galaxy clusters (Postman et al. 2012; von der Linden et al. 2014; Fu et al. 2022) including Abell 2390 (Squires et al. 1996; Okabe et al. 2010; Umetsu et al. 2009) have been conducted. These have shown masses inferred from weak lensing are consistent with X-ray mass estimates, especially for cool core clusters. For merging or disturbed clusters, mass distributions inferred from X-Ray and weak lensing are significantly different (Clowe et al. 2006). In such cases, weak lensing measurements of mass profiles are expected to be more accurate. These differences between baryonic and DM interactions during mergers can eventually be used to understand and put constraints on DM cross-section.

In weak lensing, measuring the shapes of galaxies accurately is of great importance. Traditionally, weak lensing studies have used shape measurements of galaxies made in the co-added image. However, images are obtained under a wide range of seeing conditions, cloud cover and background brightness. Depending on the science requirements, different types of weighted co-add (Zackay & Ofek 2017) are necessary for optimal measurements. It has been suggested that measuring sources in individual images would lead to better measurements since individual images can be weighted optimally to extract better shape information (Tyson et al. 2008; Jee & Tyson 2011; Mandelbaum 2018). Using measurements made in individual exposures avoids information lost in the process of co-addition and allows for small spatial scale photometry and PSF variation to be taken into account. This allows for better PSF correction which in turn leads to better shear recovery. This idea has been used in more recent weak lensing studies such as Miller et al. (2013), Zuntz et al. (2018). However, measuring sources in individual images is challenging since a vast majority of the sources are extremely faint and undetectable. We use forced measurement, a generalization of forced photometry, proposed by Dutta et al. (2024) to measure such low SNR sources. Forced measurement uses reasonable initial guess values of photon counts, shape and size of the source being measured to produce values of photon counts, shape and size that are statistically closer to the true values. The advantage of forced measurement is that it allows for the measurement of sources with S/N as low as 0.1. This allows us to measure all sources in individual images.

In this paper, we perform a weak lensing analysis of the galaxy cluster Abell 2390, a rich and massive galaxy cluster at $z=0.23$ (Abraham et al. 1996). It is a bright X-ray source and shows several arcs due to strong lensing. Abell 2390 have been extensively studied in X-Ray (Pierre et al. 1996; Allen et al. 2001; Martino et al. 2014; Sonkamble et al. 2015), optical (Abraham et al. 1996; Hutchings et al. 2002), radio (Bacchi et al. 2003; Augusto et al. 2006; Sommer et al. 2016; Savini, F. et al. 2019), weak lensing (Squires et al. 1996; Umetsu et al. 2009; Okabe et al. 2010; von der Linden et al. 2014) and strong lensing (Narasimha & Chitre 1993). In X-Ray studies (Allen et al. 2001) Abell 2390 shows hints that it has not relaxed since its last merger. Radio studies such as (Rose et al. 2024a) and (Sommer et al. 2016) have found evidence of gravitational disturbance and turbulence in Intra Cluster Medium (ICM) respectively. Weak Lensing studies have not reported any signs of merger. The paper is organized as follows. In Section 2, we describe our data and the processing pipeline. We describe strategies for co-adding our data to maximize source detection. We then measure the detected sources using a moment matching algorithm and present a novel Monte Carlo Point Spread Function (PSF) correction scheme. We describe in detail how the forced measurement algorithm is used to measure sources in individual exposures. In Section 3, we use PhoSim (Peterson et al. 2015, 2019, 2020, 2024; Burke et al. 2019) to simulate 60 one-minute exposures to show our pipeline recovers shear accurately. Two different cases with different values of input shear are tested. In Section 4, we present our results and compare them

with previous X-Ray and Radio data. We show the mass structures we recover from weak lensing correspond to an excess of light density in most regions. We also present a scheme to perform 3D mass reconstruction. In Section 5, we discuss in detail the previous studies and their results conducted on Abell 2390 using X-Ray, Radio and Optical Data. Finally, in Section 6, we show that a late stage merger scenario provides a reasonable explanation for all observed data.

2. OBSERVATIONAL DATA AND PROCESSING PIPELINE

2.1. Data Acquisition

Data for this analysis is obtained using WIYN 3.5m telescope at Kitt Peak in Arizona. The diameter of the primary mirror is 3.5m. For this study, we use the ODI instrument (Harbeck et al. 2014; Harbeck et al. 2018). It has a wide field of view, approximately $40' \times 48'$. The focal plane of the instrument is populated with 30 Orthogonal Charge Transfer Arrays CCDs (OTAs) in 5×6 configuration and has a pixel scale of $0.11'' \text{ pixel}^{-1}$. The OTAs are a kind of CCD where charges can be moved orthogonally during exposure to increase image sharpness (Harbeck et al. 2018). However, this feature was not available during our imaging sessions. Each OTA is made of 8×8 pixel cells. Each pixel cell is 480×496 pixels. In this document, we use chips to refer to pixel cells. We record images in 5 separate wide-band photometric filters u, g, r, i, and z over 6 observing runs from 2017 to 2023. The wide-band photometric filters of ODI are very similar to those used by other survey telescopes such as Sloan Digital Sky Survey (Gunn & Weinberg 1994), PanSTARRS (Kaiser et al. 2002) and DES (The Dark Energy Survey Collaboration 2005). The data obtained in the 2022 observing run was unfortunately lost due to corrupt header and metadata values. The issue is likely linked to the damage caused by the forest fires on Kitt Peak in the Fall of 2022. In total, we lost 90 images, each of 60s exposure, due to this issue. We also note one OTA, specifically OTA12 was unavailable/non-functional in 2023. Over the course of 2017 to 2023 a few CCD segments became non-functional as well. In Table 1 we show the total number of exposures, the PSF size of the co-add, and the depth of the co-add in each filter. The PSF size is defined as the median size of stars obtained using the moment matching algorithm described in Dutta et al. (2024). The depth is defined as the AB magnitude brightness of the finest source detected by SExtractor after the cuts mentioned in Section 2. We also show the number of exposures obtained in each filter in each year.

Rejecting the bad quality/unusable data, seeing conditions ranged from excellent ($0.6''$) to poor ($3''$). The poorest seeing data was obtained in the 2023 observing run which had a median seeing of $2''$. The normalized histogram of seeing in all images for the i, r, g, and z band is shown in Figure 1. The median seeing in g, r and i bands is around $1.0''$. We used the default 9-Point dithering pattern to fill the CCD gaps. In this process, the telescope pointing is shifted slightly by a pre-determined amount nine times to fill gaps between CCD and ensure uniform coverage of the field. Exposure for each image is 60s. This exposure time is reached as a compromise between short exposure time required for weak lensing (a few seconds ideally) and the 40-50 sec readout time for ODI detectors (Chang et al. 2012; Peterson et al. 2015). Short exposures are important for weak lensing since it allows one to reject or de-weight periods of bad seeing. Overall, we have 720 minutes of data divided roughly equally in each photometric band. The exposures obtained in 2017, 2020 and 2021 were on grey nights. For 2019 the exposures were obtained on a bright night and hence show significantly high background. In 2023, exposures were obtained on a dark night. We visually examined all images and rejected 36 images where satellite trail or wind shake affected the image significantly.

Photometric Band	Exposure time(s)	PSF Size (pixels)	Depth (Magnitude)	2017	2019	2020	2021	2023
u	120×60	3.6	25	22	45	18	17	18
g	161×60	3.0	26	36	45	35	27	18
r	151×60	2.9	25.5	34	45	27	27	18
i	146×60	3.0	25.5	33	43	27	25	18
z	141×60	2.9	26	35	44	26	18	18

Table 1. Observing runs (1) Photometric filter (2) corresponding exposure time, (3) PSF size of coadd. This is defined as the median size of stars when they are measured using the moment matching algorithm described in Dutta et al. (2024) (4) approximate depth of the coadd. The depth is defined as the AB magnitude brightness of the faintest source detected by SExtractor after the cuts mentioned in Section 2. The 5 right columns show the number of exposures in each filter obtained in the corresponding year. The missing years i.e. 2018 and 2022 correspond to time lost due to bad weather and technical issues. All exposures are 60s long

2.2. Correction of systematics and defects

All raw data is processed using QuickReduce (Kotulla 2013). QuickReduce, the default WIYN data processing pipeline, corrects for common systematics such as saturation and non-linearity, persistency effect, dark subtraction, flat fielding, fringing, removal of cosmic rays, and photometric calibration. Photometric calibration is done using the Pan-STARRS (Kaiser et al. 2002; Chambers et al. 2016) catalog for g, r, i and z bands while the u band is calibrated using SDSS (Gunn & Weinberg 1994) catalog. WCS match with Gaia (Brown et al. 2016) catalog is performed to obtain the final calibrated images. However, QuickReduce is not able to perfectly correct for systematics due to small but noticeable degradation of CCDs. As mentioned previously, a few CCD segments and one OTA gradually degraded and eventually became non functional over the course of 2017 to 2023. The changing nature of detector properties are hard to correct for. This was found to be true for the QuickReduce pipeline as well. This caused a noticeable amplifier glow, non-Gaussian background, unusually high or low pixel values, and cross-talk in the calibrated images. Below we discuss each of these issues in detail and how we correct for them.

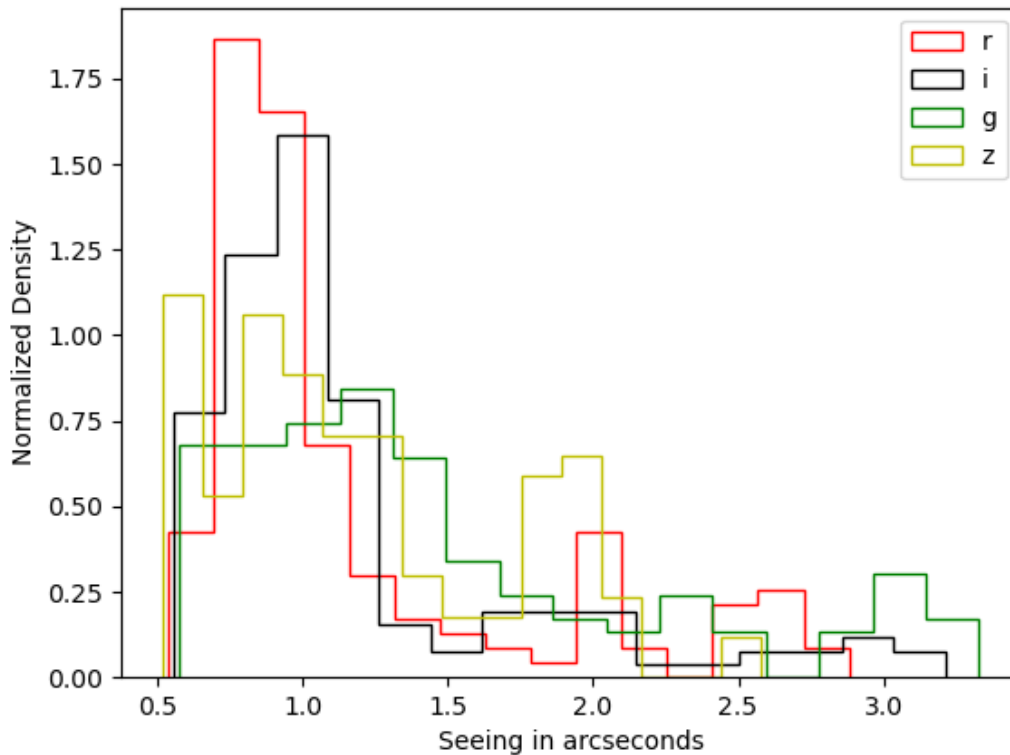


Figure 1. Normalized histogram of seeing (in arcseconds) for 151 r band, 146 i band, 161 g band and 141 z band images. We excluded the u band since the image quality is extremely poor and only a few stars are detectable in the entire image. The seeing values are the FWHM size of the stars as calculated by QuickReduce.

During visual examination of the calibrated images, it was found some chips had correlated noise. An example of this is shown in Figure 2. Such correlated noise leads to several spurious sources in the resulting co-add when employing SExtractor (Bertin & Arnouts 1996) for source detection. This limits our ability to detect faint sources. We decided to de-weight these chips during the co-add process instead of completely rejecting them. We use a weight scheme similar to Annis et al. (2014)

$$W = 100 \frac{10^{Z-25}}{(S\sigma_b)^2} \quad (1)$$

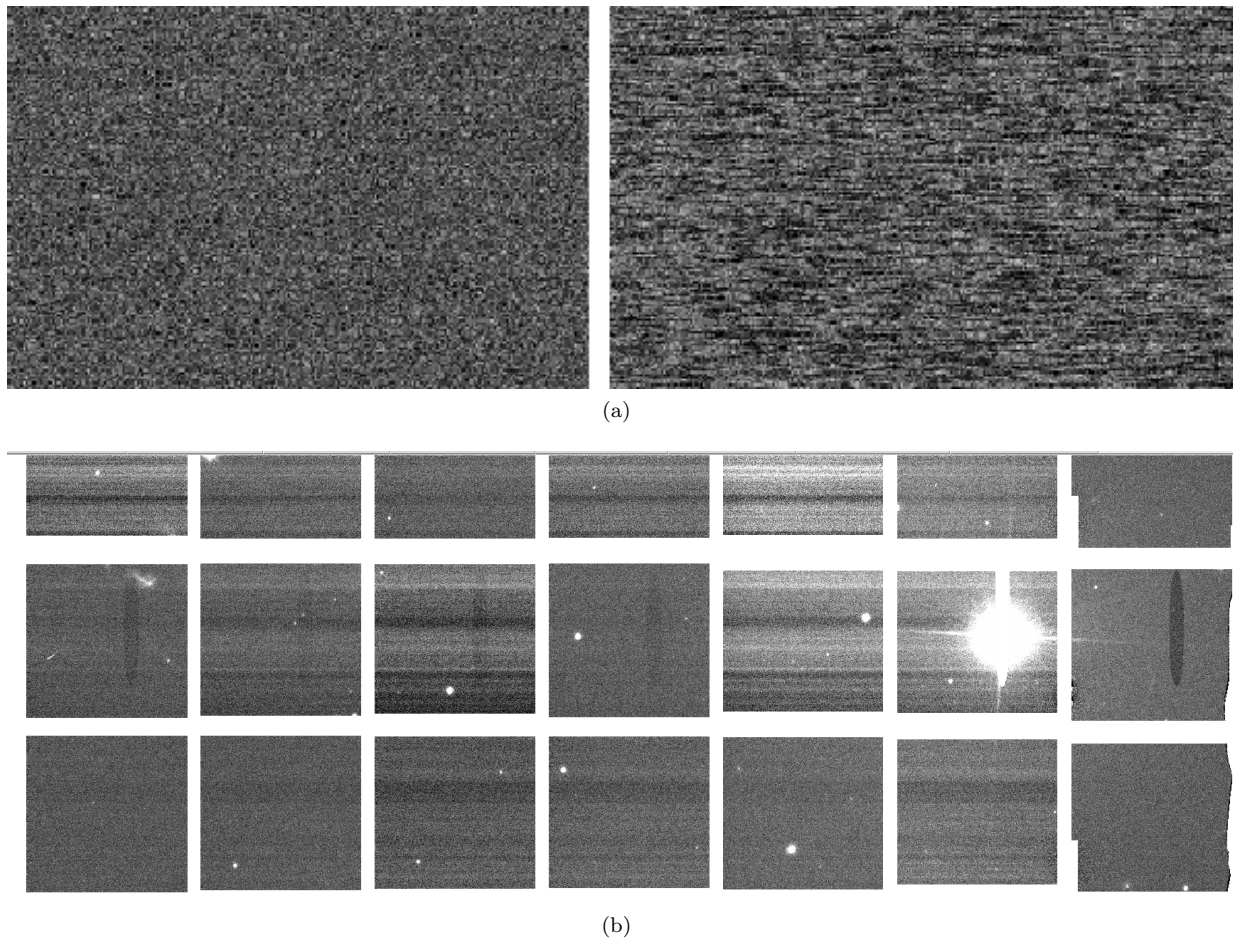


Figure 2. (a) On the left an example of background from a typical chip is shown. On the right, the background from chips with correlated noise is shown. Correlated noise gives rise to spurious sources, especially at the faint end. (b) An example of crosstalk caused by very bright sources. This image shows a portion of the OTA. QuickReduce is unable to get rid of all cases of cross-talk arising from extremely bright sources. Co-adding reduces them to a non-detectable level. However, some of the severe cases are apparent in the co-add. The vertical line of nan's through the bright source is evident.

where Z = Zero point of the image, W denotes weight, average seeing in an image is denoted by S , and σ_b is the background variance calculated using the $k=3$ sigma clipping algorithm in astropy (Astropy Collaboration et al. 2013a). This weight scheme de-weights the chips with correlated noise since those chips have higher background variance. We note that we do not completely understand the origin of such noise, but this may simply be a form of pink noise from the electronics (Hirata et al. 2024).

It was noticed that some images show significant cross-talk patterns. Due to this, pixel values are significantly higher or lower than the background in certain chips adjacent to bright sources. An example of this is shown in Figure 2b. To correct for the lower pixel values we find the lower of 6 standard deviation smaller than the background median and 0 and reject any pixels below this limit. The higher pixel values are harder to correct for since they appear intermittently and mimic real sources. Co-adding described below was able to get rid of most effects due to cross-talk. Any remaining effects are visually identified in the co-add and those regions are masked during source detection. It was also noticed some chips have background variation significantly higher than expected from Poisson statistics. Most of these chips have imperfections and limit our ability to detect extremely faint sources in the co-add. The problem is severe enough that the weighting scheme and cuts presented above were not able to effectively de-weight these chips. To exclude these chips we perform cuts in the background median vs variance space. We use the median instead of the mean because it was found to be much more stable. A graph showing the distribution of median vs variance of the background for all chips in g, r, and i band is shown in Figure 3. Both background median and variance are obtained

after $k=3$ sigma clipping. We consider the condition

$$0.9 \times \text{Median} \leq \text{Variance} \leq \text{Median} + 300 \quad (2)$$

where variance is the background variance and median is the background median obtained after $k=3$ sigma clipping. If a chip violates this condition in more than half the images, the chip is flagged problematic and its weight is set to 0 for all images. This condition effectively rejects the problematic chips.

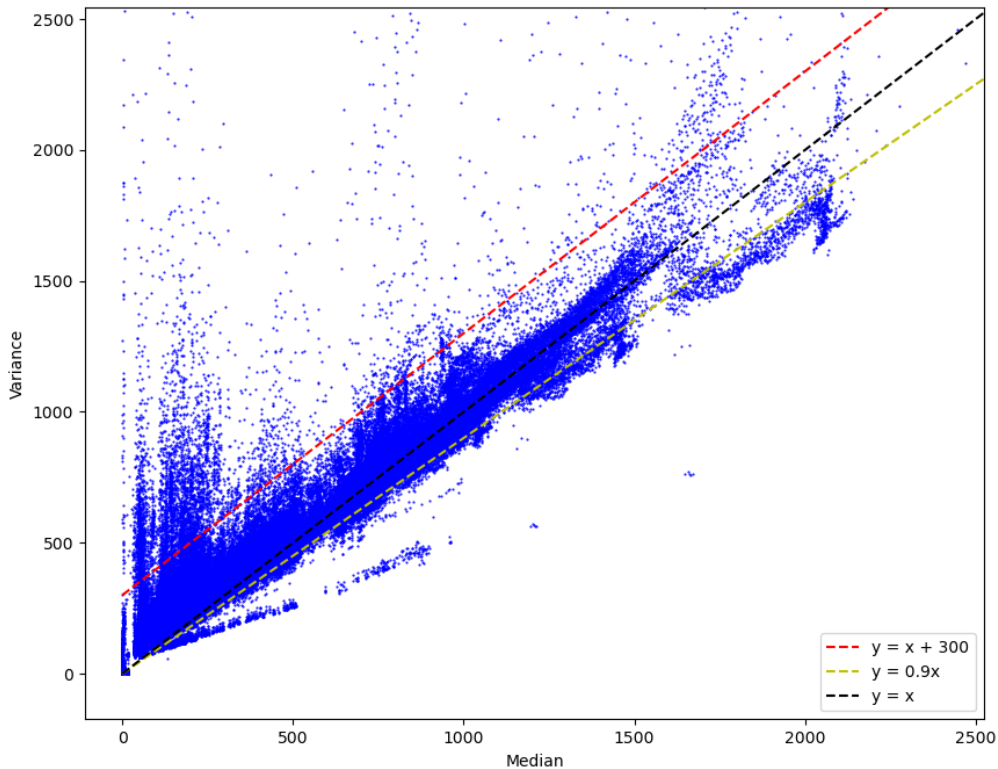


Figure 3. Median of background photon counts vs variance of background photon counts for all chips in every image in g, r, and i band. Shown in red is the $y = x + 300$ while the black line is $y = x$. The yellow line shows $y = 0.9x$ line. If a chip is outside the strip which is defined by the red and yellow lines in over half the images, the chip is rejected. This condition was found to be effective in identifying severely defective chips.

2.3. Co-adding and Source Detection

The co-adds were performed for each of the five photometric bands separately using the software SWarp (Bertin et al. 2002). SWarp settings used are listed in Table 2. The i and r band images were co-added further. The color image of the entire field is shown in Figure 4. The i+r coadd image was inspected visually for any additional imperfections. A few regions of defects were visually identified. Most of these defects come from clumps of unusually high pixel values. We do not understand the origins of these pixels but they tend to appear at the chip edges or in chips with pre-existing defects. There is also a small amount of cross-talk noise from a few extremely bright stars in the field. We mask out these regions to limit spurious detection. The total percentage of area masked out was less than 2%. This is the final image used for source detection. We employed SExtractor (Bertin & Arnouts 1996) to detect sources. The SExtractor settings used is shown in Table 2. These settings were found to give us the maximum number of sources without contaminating the sample with too many spurious detections. The details of the number of images co-added and the

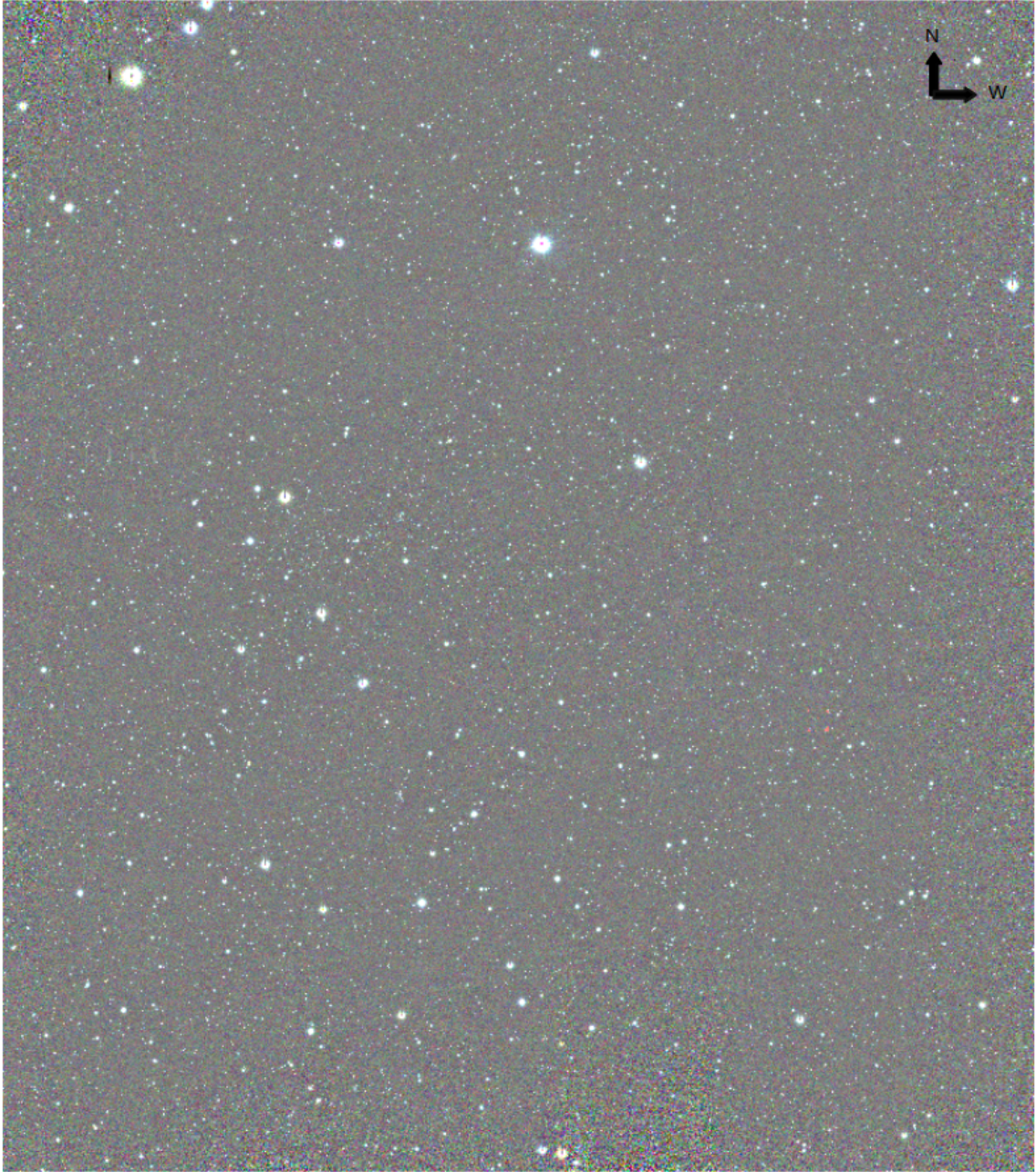


Figure 4. RGB Color image of the full field containing the galaxy cluster Abell 2390. We use the co-added images in z, i and r band. They respectively correspond to R, G and B channels. The field of view is approximately $43' \times 49'$.

depth and PSF size of the final image are shown in Table 1. The final number of sources detected in the i+r co-added image is 54059 and density is $\sim 31.8 \text{ arcminute}^{-2}$.

2.4. Co-add Measurement and Source Classification

The sources detected in the previous step are measured using the moment matching algorithm developed originally by Kaiser et al. (1995) and later modified by Bernstein & Jarvis (2002). We use an adaptive moment matching algorithm with elliptical Gaussian weights. The shape and size of the weight is the best fit elliptical Gaussian for the source being measured. The weighted second moments are calculated as

$$Q_{ij} = \int \theta_i \theta_j f(\theta_i, \theta_j) W(\theta_i, \theta_j) d\theta_i d\theta_j \quad (3)$$

Keyword	Value
WEIGHT_TYPE	MAP_WEIGHT
COMBINE_TYPE	WEIGHTED
RESAMPLING_TYPE	LANCZOS3
SUBTRACT_BACK	Y
BACK_TYPE	AUTO
BACK_SIZE	256
BACK_FILTERSIZE	2
RESCALE_WEIGHTS	Y

Keyword	Value
DETECT_MINAREA	5
DETECT_THRESH	0.8
ANALYSIS_THRESH	0.8
FILTER	Y
FILTER_NAME	<i>gauss_11.0_13x13.conv</i>
DEBLEND_NTHRESH	64
DEBLEND_MINCONT	0.0001
CLEAN	Y
CLEAN_PARAM	2.0
WEIGHT_TYPE	MAP_WEIGHT
BACK_TYPE	AUTO
BACK_VALUE	0.0
BACK_SIZE	128
BACK_FILTERSIZE	2

Table 2. List of SWarp parameters used on the left and list of SExtractor parameters used on the right.

where θ represents generalized co-ordinates, $W(\theta_i, \theta_j)$ is the weight function and $f(\theta_i, \theta_j)$ is the cutout of the source. The polarization or ellipticity parameters are then defined as

$$e_1 = \frac{Q_{11} - Q_{22}}{Q_{11} + Q_{22}} \quad e_2 = \frac{2Q_{12}}{Q_{11} + Q_{22}} \quad (4)$$

where e_1 represents elongation along x (positive values) and y axes (negative values) and e_2 represents elongation along $y = x$ or $y = -x$ lines. Traditionally the quantities Q_{11} , Q_{22} and Q_{12} is referred as σ_{xx}^2 , σ_{yy}^2 and σ_{xy}^2 respectively. This algorithm was modified to produce the photon counts, centroid, size of the source along with ellipticity. We chose the best-fit elliptical Gaussian as our weight function. For a detailed description of this algorithm see [Dutta et al. \(2024\)](#).

The measurements are done in the i+r co-add image. In the first step, the optimal cutout size of each source was determined. To estimate the optimal cutout size, a rough guess of size from SExtractor, $S_{sextractor}$ is made.

$$S_{sextractor} = \sqrt{X2IMAGE + Y2IMAGE} \quad (5)$$

where $X2IMAGE$ is the isophotal image second order moment in x and similarly $Y2IMAGE$. The second order moments are obtained from the SExtractor output file. This estimated size is set at 25% larger than SExtractor size. The lower limit of estimated size was capped at 4 pixels. Next a square cutout with side length 8 times the estimated size is made to measure sources. It was found that in rare cases the moment matching algorithm fails when it is run on such a cutout. However, the algorithm successfully converges when a smaller cutout is made. This happens typically due to light contamination from other nearby sources, leading to gross mis-estimation of background. For cases where the algorithm initially fails, we reduce the size of the cutout by 2 pixels along the x-axis and 2 pixels in the y-axis symmetrically from each side. This is repeated until the algorithm successfully converges or the cutout is less than or equal to 24x24 pixels. This is the minimum size of cutout needed to measure a source. Using this method we obtain a good estimate of the optimal cutout size.

Next, we attempt to reduce the effect of light contamination from nearby sources, thus increasing the accuracy of our measurements. First, we calculate the bound flag (*bndflag*) using the previous measurements. Flags are calculated using the method outlined in Section 2.6. If the bound flag is raised, it indicates that there is a significant chance that the background estimation might be affected by nearby sources which in turn affects the flux estimation. To correct for this we use two strategies:

1. The cutout is moved by 3 pixels in a direction 180° away from the nearest source
2. During the iterative process of moment matching, the background is fixed. To determine the value of background we select three 4x4 pixel regions. These regions are $s/\sqrt{2}$ away from the central pixel of the cutout, where s is the side length of the cutout. The three regions selected are 90° , 180° and 270° away from the line joining the

source to its nearest source. We also create a 4x4 array of zeros. The array of zeros was to ensure the background value does not wander too far from the truth which is very close to 0 in the co-adds. The median value of these 64 pixels in four 4x4 cutouts is the fixed background value.

If the bound flag is not raised, we shift the cutout 3 pixels away from the nearest source and re-measure it using the moment matching algorithm. It was found that the amount of shift is not important as long as the shift is small compared to the size of the cutout. We repeat the same measurement process for the co-add in each of the 5 photometric bands. The flux vs size graph from the i+r co-add band measurements for all sources is shown in Figure 5. The vertical column feature arises from stars which have approximately fixed size (size of the PSF) but vary in magnitude. Having a clean sample of stars to measure PSF from is the first step in accurate PSF estimation. We cross-referenced all sources in our field with the star catalog from Gaia EDR3 (Brown et al. 2021). The criteria used for matching was the difference in WCS coordinates of the source in our catalog and Gaia catalog be less than $0.72''$. The sources that were matched are shown as red points in Figure 5a. This gives us an extremely clean sample of stars to determine PSF.

While stars are useful for determining PSF, they are not useful for weak lensing purposes and only serve to dilute the shear signal. Hence an important aspect of any weak lensing pipeline is accurately rejecting stars. In our case rejecting only the stars cross-matched with Gaia EDR3 is not enough. Gaia EDR3 goes to a depth of magnitude 21 in the g band while our i+r co-added image has a depth of magnitude 26. The mismatch in the depth of the two catalogs means that several fainter stars in our field cannot be cross-matched with the Gaia catalogs. Hence, we visually identified the vertical star strip shown as a black box in Figure 5a. Any sources inside the black box were rejected from weak lensing analysis. We note that this method is not perfect and some fainter stars outside the black bounding box enter our galaxy sample. To reject extremely bright sources that show brighter fatter effect, any sources brighter than magnitude 15 shown by the horizontal yellow line were rejected. We also reject any sources with size ≥ 12 pixels. These most likely arise from severe blending. This value was selected somewhat arbitrarily and changing this limit does not significantly affect our analysis. We also wish to reject sources that have size $3\epsilon_{PSF}$ below the median PSF value, where ϵ_{PSF} is the variation of PSF in the image. This is shown by the yellow line on the left in Figure 5a. All sources left of this yellow line are rejected. A method to determine ϵ_{PSF} is described in the next section. These are likely spurious sources arising from cosmic rays or defective pixels. After these cuts, we have 45022 sources remaining corresponding to a source density of $26.5 \text{ arcminute}^{-2}$.

To calculate photometric redshift we use the magnitude brightness measured in the co-add of the five photometric bands. We use these as inputs to EAZY (Brammer et al. 2008) to determine photometric redshift. A few random galaxies across our field were selected and the photometric redshift was compared to the spectroscopic redshift obtained from the NASA Extragalactic Database (NED). These were generally found to be in good agreement.

2.5. PSF correction

PSF causes dilution in the ellipticity and shear signals and hence needs to be corrected. It has also been shown PSF variation across the image can masquerade as shear signal if not taken into account. PSF correction is done in two steps. First, we interpolate the PSF across the image and then in the second step we correct the shape and ellipticity dilution due to PSF. In any astronomical image, PSF can only be precisely determined only at locations where stars are present. To determine the exact PSF shape at other locations a variety of methods can be found in literature. Van Waerbeke et al. (2002) used second order polynomial to model PSF variation across an image. Other elaborate methods have been proposed by Hoekstra (2004), Bergé et al. (2011) and Chang et al. (2012). We use an inverse distance weight interpolation, similar to one described by Gentile et al. (2012) because of its simplicity and performance. To find $\sigma_{xx}^2(PSF)$ we use

$$\sigma_{xx}^2(PSF) = \sum_{i=1}^n \sigma_{xx,i}^2 w(i) \quad (6)$$

where $\sigma_{xx,i}^2$ is the measured Q_{11} of the i-th star obtained from the moment matching method, and n is the number of stars used. The weight $w(i)$ is defined as

$$w(i) = \frac{1/d_i}{\sum_i 1/d_i} \quad (7)$$

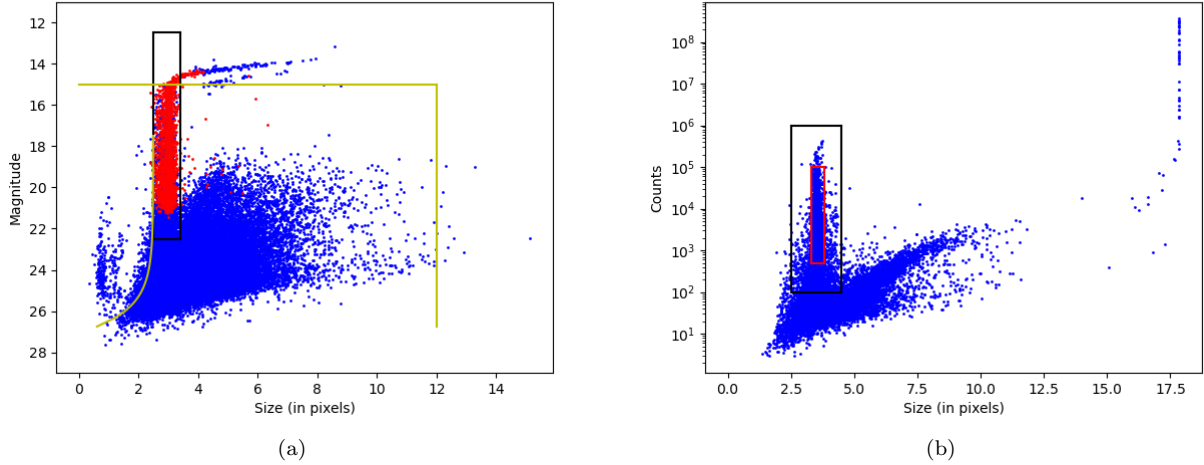


Figure 5. (a) Magnitude vs size for sources detected and measured in the $i + r$ co-add. The points shown in red are stars matched with the Gaia EDR3 catalog. All sources inside the black box are rejected from the weak lensing analysis pipeline. So are the sources above the horizontal yellow line (15th magnitude) to account for brighter fatter effect. Sources to the right of the vertical yellow line are rejected to avoid blended sources and artifacts. Sources to the left of the curved yellow line are also rejected since these are 3 standard deviations smaller than the median PSF. (b) The photon counts vs size graph for the $i+r$ co-added image simulated using PhoSim for the first case of $\gamma_1 = 0.1$. The points in the red box are used for PSF interpolation. The points inside the black box are not used for the shear analysis. The condition for the red box is $3.3 < \text{size} < 3.8$ pixels and $500 < \text{counts} < 10^5$. For the black box the conditions are $2.5 < \text{size} < 4.5$ pixels and $10^2 < \text{counts} < 10^6$.

where d_i is distance of the i -th star from the source. We found the number of stars selected for PSF correction in the range $n=5$ to $n=25$ does not affect our analysis significantly. We selected $n = 15$. Similar process is followed for interpolating $\sigma_{xy}^2(PSF)$ and $\sigma_{yy}^2(PSF)$. This completes PSF interpolation.

A significant portion ($\sim 35\%$) of these sources are measured to have a size smaller than PSF. Clearly, these measurements are un-physical. Traditionally sources smaller than PSF have been rejected (Gruen et al. 2013; Applegate et al. 2014; McCleary et al. 2020). However, these sources contain a large amount of information which would be lost if we reject these sources. The measurement of size being smaller than PSF is simply due to statistical fluctuations. In other words, the size of both PSF and sources have Poisson noise and other systematic effects which give rise to size measurements that are smaller than PSF. We introduce PSF correction using a novel Monte Carlo method. If we assume an elliptical Gaussian profile for both the source and PSF, true σ_{xx}^2 of the source is

$$\sigma_{xx}^2(true) = \sigma_{xx}^2(measured) \pm \sqrt{\frac{S^4}{N}(1+K)} - \sigma_{xx}^2(PSF) \pm \epsilon(xx)_{PSF} \quad (8)$$

where $\sigma_{xx}^2(true)$ is the true value, $\sigma_{xx}^2(measured)$ is the measured value, $\sigma_{xx}^2(PSF)$ is the value for PSF and $\epsilon(xx)_{PSF}$ is the error in PSF value. The expression $\sqrt{S^4(1+K)/N}$ is the Poisson error in $\sigma_{xx}^2(measured)$ as shown by Dutta et al. (2024), where S is measured size, N is measured photon counts and K for elliptical Gaussian case is $4\pi S^2 B/N$. B is the background level. In order to find the error in PSF, $\epsilon(xx)_{PSF}$ we use the bright stars where the Poisson error is negligible. For the co-adds it was found the stars matched with the Gaia catalog are bright enough to neglect the Poisson error. This is also clear from Figure 5a where the red points show a constant width. This width corresponds to PSF variation due to turbulence and other systematics. We perform a $k=3$ sigma clip for $\sigma_{xx}^2(measured)$, $\sigma_{yy}^2(measured)$ and $\sigma_{xy}^2(measured)$ to reject any stars with significant blending. Stars brighter than magnitude 15.75 are rejected to avoid brighter fatter effect. This threshold is a factor of 2 lower than the threshold mentioned in the previous section. This is to ensure the star sample is well away from the limits at which brighter fatter becomes important. We also reject stars with *bflag* or *vflag* raised. The calculation of flags is presented in Section 2.6. The other flags are not considered since the stars matched with Gaia is fairly bright. Of the remaining stars, we find $P_{84} - P_{16}$ for σ_{xx}^2 , where P_i represents the i -th percentile. This value corresponds to two standard deviations i.e. one standard deviation from the median value on either side. Half of this value is defined as $\epsilon(xx, Turbulence)_{PSF}$. This gives only the typical

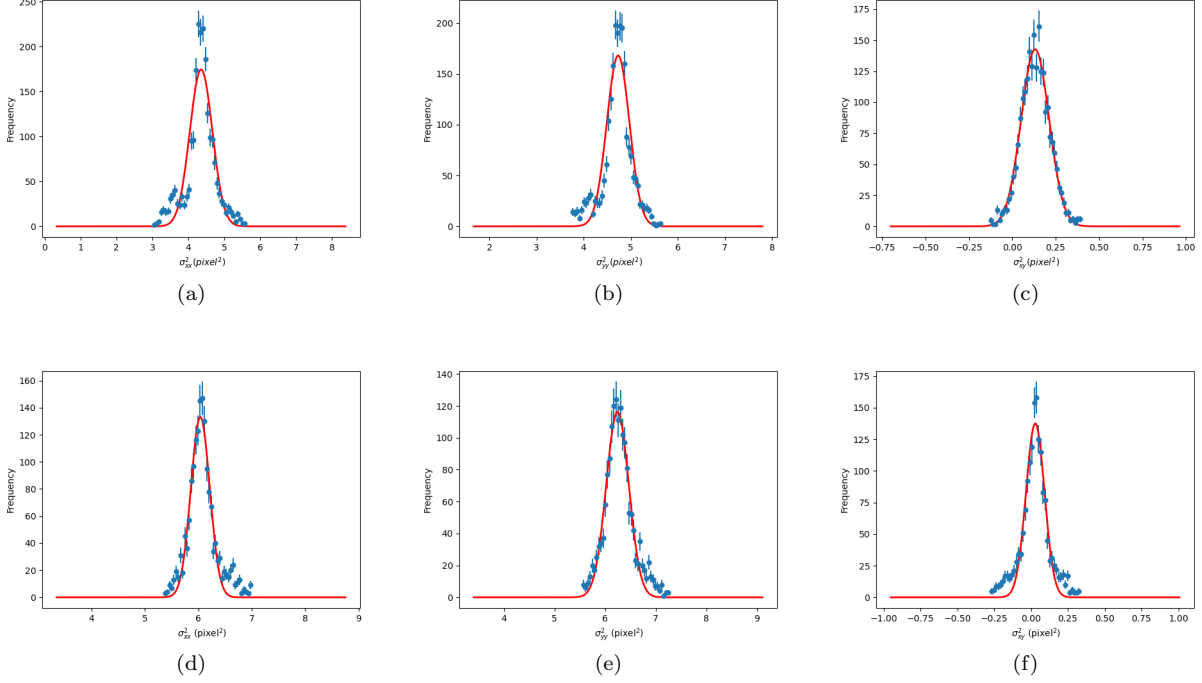


Figure 6. (a) The points show the σ_{xx}^2 of stars in the i+r co-added image. The red curve shows the best fit Gaussian obtained with a width half the value of $P_{84} - P_{16}$ where P_i represents the i-th percentile value. The fits are reasonably good though not perfect. (b) and (c) shows similar graphs for σ_{yy}^2 and σ_{xy}^2 . The widths of the Gaussians are 0.37, 0.27 and 0.08 respectively. (d) The points show the σ_{xx}^2 of stars in the i+r co-added image simulated using PhoSim for the first case i.e. $\gamma_1 = 0.1$. The red curve shows the best fit Gaussian for each case. (e) and (f) show similar graphs for σ_{yy}^2 and σ_{xy}^2 . The width of the Gaussians are 0.18, 0.22 and 0.06 respectively.

error across the frame due to turbulence. In Figure 6a, 6b and 6c the histograms of stars used for PSF interpolation are shown. The red curve is a Gaussian centered on the median with a width equal to $\epsilon(xx, Turbulence)_{PSF}$.

To the turbulence error, we add the Poisson error of the stars used for PSF interpolation. Using the errors presented in (Dutta et al. 2024) and standard error propagation, the PSF error due to Poisson noise is

$$\epsilon^2(xx, Poisson)_{PSF} = \sum_{i=1}^n w^2(i) \left(\frac{S^4(i)}{N(i)} + \frac{4\pi BS^6(i)}{N^2(i)} \right)^2 \quad (9)$$

where $S(i)$ is the size of the i-th star and $N(i)$ is the photon counts of the i-th star. The Poisson and the Turbulence component are added in quadrature to find $\epsilon(xx)_{PSF}$. It was found the turbulence component always dominates in the co-adds and is an order of magnitude larger than the Poisson component.

Now we have determined all the terms on the right-hand side of Equation 8. To find $\sigma^2(true)$ we perform 30k iteration of the Monte Carlo equation 8. In each iteration, the errors are randomly sampled from a Gaussian distribution with mean 0 and standard deviation being the error value. This includes both Poisson error of both the source and the PSF and uncertainty in PSF arising turbulence, instrument, and optics. In each iteration sampling is done for σ_{xx}^2 , σ_{yy}^2 and σ_{xy}^2 . We only consider the cases where the following conditions are satisfied

- $\sigma_{xx}^2(true) > 0$
- $\sigma_{yy}^2(true) > 0$ and
- $2\sigma_{xy}^2(true) < \sigma_{xx}^2(true) + \sigma_{yy}^2(true)$

The first two conditions ensure the size along the x and y axes individually are positive and hence the overall size is positive. The last condition ensures $|e_2| < 1$. We take median values of σ_{xx}^2 , σ_{yy}^2 and σ_{xy}^2 in all the iterations that

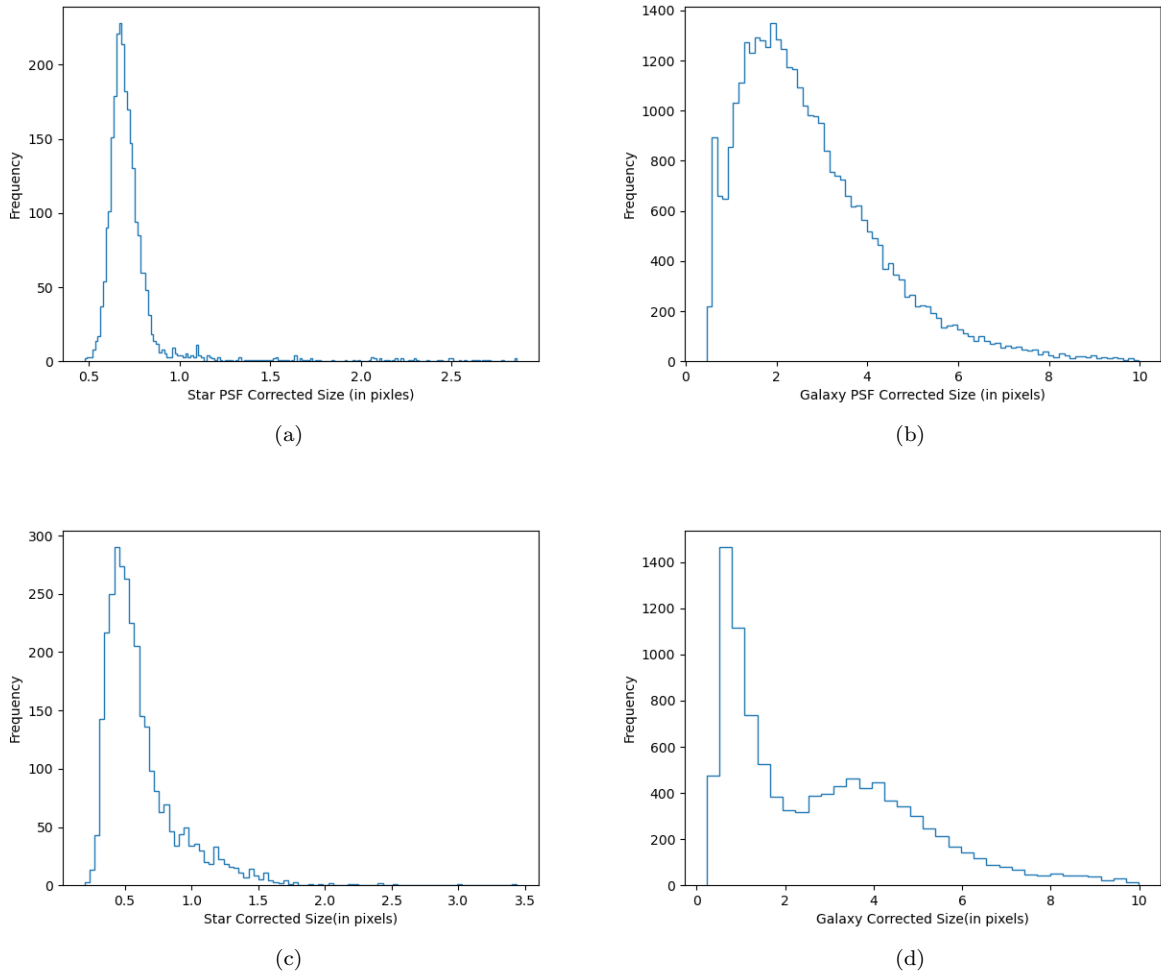


Figure 7. (a) and (b) The plot on the left shows the histogram of all stars after they have been passed through the Monte Carlo PSF correction method in the i+r co-added image. Sigma clipping is necessary to reject the stars on the right tail which are not suitable for calculating PSF. The graph has been truncated $x = 3$ pixels. A similar graph for galaxies is shown on the right. This graph has been truncated at $x = 10$ pixels. (c) and (d) On the left histogram of all stars after they have been passed through the Monte Carlo PSF correction method in the i+r co-added images simulated using PhoSim with input $\gamma_1 = 0.1$ is shown. The plot is truncated at $x = 3.5$ pixels. Not all stars shown in the histogram are used for PSF correction. Sigma clipping is required to reject the stars on the right tail which are not suitable for calculating PSF. A similar graph for galaxies is shown on the right. This plot is truncated at $x = 10$ pixels.

satisfy these conditions to find $\sigma_{xx}^2(true)$, $\sigma_{yy}^2(true)$ and $\sigma_{xy}^2(true)$. We note the conditions listed above were found to be optimal. Several sets of conditions such as constraining overall size > 0 and constraining $|e_1| < 1$ were tried and rejected. Sources in which less than 50 samples satisfy the above conditions are considered to have failed PSF correction. Figure 7a and 7b show size histograms of stars and galaxies after PSF correction has been performed in the i+r coadd.

2.6. Flags

In this section, we describe the different flags used in this paper and the conditions that raise these flags. These flags are primarily used to determine which measurements are likely to be contaminated. For instance, sources that lie close to a chip edge or in chip gaps would need to be rejected. Sources that have a very small spatial separation or are blended would likely yield contaminated measurements as well. Below we list all the flags used and the conditions that trigger the flag.

1. Vertical Flag (*vflag*): Some brighter stars have a vertical array of zeros near the center. This can be seen in Figure 2b. These stars are unsuitable for PSF determination. Let us assume the center of the source is at pixel (x_c, y_c) . The *vflag* is raised if any of the following conditions is satisfied

- Calculate the average pixel value in a horizontal 3x1 pixel strip two pixels above y_c . In other words the mean value of pixels at $(x_c - 1, y_c + 2)$, $(x_c, y_c + 2)$ and $(x_c + 1, y_c + 2)$ is calculated. The mean value of pixels at $(x_c - 6, y_c + 2)$ and $(x_c + 6, y_c + 2)$ is also calculated. If the first quantity is less than either of the second then the flag is raised.
- Similar calculation as before except we consider a strip three pixels above y_c . We find the mean value of pixels at $(x_c - 1, y_c + 3)$, $(x_c, y_c + 3)$ and $(x_c + 1, y_c + 3)$. The mean value of pixels at $(x_c - 7, y_c + 3)$ and $(x_c + 7, y_c + 3)$ is also calculated. If the former quantity is smaller than either of the latter, the flag is raised.

2. Bad Flag (*bflag*): As mentioned before some sources at the edges of CCDs or in chip gaps need to be rejected. We check if the cutout is at least 6 times the expected size of the source in that image. It was found this is the minimum cutout size required to recover flux, shape and ellipticity accurately. The expected size is calculated using

$$\sigma_{image}^2 = \sigma_{coadd}^2(true) + \sigma_{image}^2(PSF) \quad (10)$$

where $\sigma_{coadd}^2(true)$ is obtained after using the Monte Carlo method described above to solve Equation 8 in the i+r co-add. The interpolated values of the PSF in the individual image is $\sigma_{image}^2(PSF)$. In this equation σ^2 can be substituted with σ_{xx}^2 , σ_{yy}^2 or σ_{xy}^2 . The expected size is

$$S = \sqrt{\sigma_{image,xx}^2 + \sigma_{image,yy}^2} \quad (11)$$

If the cutout size is larger than 6 times the expected size of the source, then we check for pixel values ≤ 0 inside a square box of side 6 times the size. If found, this flag is raised i.e. set to 1. If the initial cutout size is less than 6 times the size of the source being measured, any pixel value ≤ 0 in the cutout would trigger this flag. This flag is exclusively used for cutouts made in individual frames.

3. Background Flag (*bkflag*): This flag is used in the i+r co-add. We use the larger of σ_{xx}^2 or σ_{yy}^2 to find the size. Size is defined as $S = \sqrt{\sigma_{xx}^2 + \sigma_{yy}^2}$. In this case σ_{xx}^2 and σ_{yy}^2 are the values measured by the moment matching method and not corrected for PSF. We replace the smaller of the two with the larger. We also find the average value of background standard deviation in the full image and call this global standard deviation σ_g . Next, assuming an elliptical Gaussian profile, we find the radius at which light from the source becomes equal to the background standard deviation. We denote this as r .

$$r = \sqrt{S^2 \log \left(\frac{2\pi S^2 \sigma_g}{N} \right)} \quad (12)$$

where N is the photon counts and S is the size. We also define $r_1 = r/\sqrt{2}$. We now define 8 regions. The first four regions are simply a 4x4 pixel square at the corners of a square with a size length $2r$. The next four regions are similar except now they are at the corners of a square of side length $2r_1$. We find the median value in each region. We also find the median value of the eight median values and call this local median. If the local median is higher than the global median + 2 times the global standard deviation, the flag is raised. We also count the number of regions whose median value is greater than the local median + 1.5 times the local standard deviation or lower than the local median - 1.5 times the local standard deviation. If more than one region exceeds this threshold, then the flag is raised as well.

4. Bound Flag (*bndflag*): We calculate the r for all sources as described above. We cap the lower value of r at 13 pixels. This number is decided since it is just larger than half the size of the minimum cutout of 26x26 pixels. For every source, the distance of the source centroid from the centroid of all other sources is calculated. If the centroid distance is lower than the sum of the r for each pair considered, the flag is raised. This flag indicates if a significant amount of light from a source is present in the cutout of another source. Fewer than 2% of our sources were found to raise this flag. However, it was also found that this flag was not adequate in some cases because, for most astronomical sources, light falls off slower than a Gaussian.

2.7. Measurement in Individual Images

It has been suggested using measurements made in individual images over co-adds could lead to better measurements (Tyson et al. 2008; Jee & Tyson 2011; Mandelbaum 2018). This is because co-adding causes loss of information and averaging of systematic effects. In theory, measurements in individual images can be better corrected to take systematic into account. Measurements made in images with better seeing and lower background brightness can also be given more weight. Indeed, this idea has been used in some recent weak lensing studies such as Miller et al. (2013), Zuntz et al. (2018). However, the challenge with such a scheme is that the sources will be extremely faint in each individual image. In all studies to date, measurements in individual images are performed only when the source has high enough S/N (~ 10 or more). To get around this limitation, we use forced measurement (Dutta et al. 2024) which is capable of measuring sources with $\text{SNR} \ll 1$. The details of this algorithm is beyond the scope of this paper, but we describe it here briefly. Forced measurement is a generalization of forced photometry (Lupton et al. 2001; Stoughton et al. 2002; Lang et al. 2016). Using the moment matching algorithm described above, we can measure the shapes and position of the detected sources in the co-add. Next, we can use this measurement as our initial guess and run the moment matching algorithm for a single iteration, as opposed to convergence. The flux measurements obtained from this method are identical to forced photometry and so it stands to reason, that the centroid and shapes found could hold some information. This was found to be true and is the essence of forced measurement. First, the pixel values after background subtraction are truncated in a fashion that makes all pixel values positive. This step is crucial to ensure that measured σ^2 values are not negative. Then we use a method similar to forced photometry, where we use the expected shape and size of the source to perform a single iteration of the moment matching algorithm. The values of flux shapes and sizes thus obtained are corrected to take into account the effect of truncation. The details of this algorithm have been described in Dutta et al. (2024).

We decided to perform measurements only in g, i, and r band individual images since almost all sources detected in the co-add can be detected in these individual band co-adds as well. To estimate the PSF in individual exposures, a 80×80 pixel cutout at the location of the stars is made and moment matching measurement is done on these cutouts. To discard any stars with defects or blending we perform $k=3$ sigma clip of all the stars in σ_{xx}^2 , σ_{yy}^2 and σ_{xy}^2 . Bright stars with $\text{SNR} \geq 100$ and no flags raised are selected for PSF estimation. To avoid brighter fatter effect any star having $\geq 10^6$ photon counts is rejected. We also reject any stars in chips where the weight has been set to 0 during co-addition. This produces a very pure sample of stars to determine PSF. Interpolation of PSF is done using Equation 6.

For the remaining sources, a square cutout 8 times the size of the source is created with the source at the center. To check whether the source is bright enough for the moment matching algorithm to converge, the approximate SNR is calculated. It has been shown in Dutta et al. (2024) when $\text{SNR} \geq 15$ convergence is guaranteed. SNR is defined as

$$\text{SNR} = \frac{N}{\sqrt{N + 4AB}} \quad (13)$$

where N is the photon counts from the source, A is the area and B is the background. The background is taken from the header and is the global median sky background. An alternate approach to determine if the source is bright enough for moment matching to converge would be to run the measurement algorithm on the cutout to check for convergence. However, this approach suffers from the fact that it would be challenging to differentiate between the case where the source is bright enough for convergence and the algorithm converging on a nearby bright source or defect. Hence, this approach was not explored further. Calculating the SNR before actually measuring the source is not possible. Hence, the SNR calculation is done using the expected size, expected flux and overall background of the image. Expected flux (N_{expected}) and expected size (σ_{image}^2) is calculated as

$$N_{\text{expected}} = N_{\text{coadd}} \times \left\langle \frac{N_{\text{image}}(\text{star})}{N_{\text{coadd}}(\text{star})} \right\rangle \quad (14)$$

$$\sigma_{\text{image}}^2 = \sigma_{\text{coadd}}^2(\text{true}) + \sigma_{\text{image}}^2(\text{PSF}) \quad (15)$$

where $\sigma_{\text{coadd}}^2(\text{true})$ is obtained after using the Monte Carlo method described above to solve Equation 8 in the i+r co-add. The interpolated values of the PSF in the individual image is $\sigma_{\text{image}}^2(\text{PSF})$. In this equation σ^2 can be substituted with σ_{xx}^2 , σ_{yy}^2 or σ_{xy}^2 . The expected photon counts of a source in an image is N_{expected} , N_{coadd} is the photon counts of the source in the corresponding band co-add and $\langle N_{\text{image}}(\text{star})/N_{\text{coadd}}(\text{star}) \rangle$ is the ratio of photon

counts of stars in the image to photon counts in the co-add. The angle brackets in the above equation indicate the median. To find the median value, only the stars that are used for PSF interpolation at the given location are utilized. This was done to minimize the effect of photometric variation across the image.

If SNR is lower than 15, we use forced measurement (Dutta et al. 2024). Forced measurement requires a reasonably good starting guess. We use $N_{expected}$ and σ_{image}^2 from the above equations as guess values for forced measurement. After forced measurement has been performed, we similarly perform Monte Carlo PSF correction as before. A slightly modified Monte Carlo equation shown in Equation 17 is used to take into account that the errors in the flux, shape, and size obtained from forced measurement are significantly tighter than Poisson errors. This arises from the fact that forced measurement needs a reasonable guess to start with and only a single iteration is performed. The error in the measured parameters are calculated as

$$\epsilon_{\sigma_{xx}^2} = p_{\sigma_{xx}^2}(N, S, B) \sqrt{\frac{S^4}{N} + 4\pi S^2 B \frac{S^4}{N^2}} \quad (16)$$

where N is photon counts i.e $N_{expected}$, S is size and B is the background value and $p_{\sigma_{xx}^2}$ is a function of $N_{expected}$, S and B . We use the piece wise linear function of $p_{\sigma_{xx}^2}$ from Dutta et al. (2024). All successful measurements are passed through the Monte Carlo PSF correction scheme similar to Equation 8. For individual exposures the PSF correction equation for σ_{xx}^2 is

$$\sigma_{xx}^2(true) = \sigma_{xx}^2(measured) \pm p_{\sigma_{xx}^2} \sqrt{\frac{S^4}{N}(1+K) - \sigma_{xx}^2(PSF)} \pm \epsilon(xx)_{PSF} \quad (17)$$

where $\sigma_{xx}^2(measured)$ is the measured values in individual exposures by forced measurement. In cases where the moment matching method successfully converges, $p_{\sigma_{xx}^2}$ is set to 1. The error in PSF is $\epsilon(xx)_{PSF}$. Similar equation is used to determine $\sigma_{yy}^2(true)$ and $\sigma_{xy}^2(true)$. We perform 30k iterations and use the same condition used in the co-add PSF correction to select which iterations are considered valid. Sources for which less than 50 samples satisfy the above conditions are considered to have failed PSF correction.

2.8. Combining Data from Individual Images to get Shear

The individual frame measurements of each source need to be combined into a single shape and ellipticity measurement. To reject contaminated measurements, we apply some sensible cuts. We reject all measurements where any flag has been raised either in the i+r co-add or individual frames. Sources where the size is over a factor of 2 larger than the i+r co-add size after PSF correction is rejected. If this condition fails, it is a strong indication that the source was not measured accurately. We reject measurements where the flux value is negative or nan. This is because negative or nan values do not make physical sense. Cases, where PSF correction failed in single frames and cases where forced measurement produces nans, are rejected as well. Finally, to ensure defects and noise do not affect our measurements, we calculate the sigma-clipped median and standard deviation of individual frame flux measurements in a filter. Any measurement where the flux is 3 standard deviations away from the median is rejected. This is to ensure defects like ‘stripes’ shown in Figure 2a do not influence the measurement of faint sources. We also reject images with $\sigma_{xx}^2(PSF)$ or $\sigma_{yy}^2(PSF)$ greater than 30 pixel² which corresponds to a size of approximately 7.7 pixels i.e. a seeing FWHM of 2.6''. Weak lensing analysis requires very stringent PSF cuts and images with seeing larger than 1'' have traditionally been discarded (Gruen et al. 2013; Okabe et al. 2010). Also at approximately 4'' seeing, point sources start to form donut shapes indicating the telescope is extremely out of focus. We also reject images where the sigma clipped standard deviation in stellar $\sigma_{xx}^2(PSF)$ or $\sigma_{yy}^2(PSF)$ is greater than 3 pixels. This corresponds to an unusually large variation of PSF across the field and is indicative of issues with the image. These conditions are not mutually exclusive.

The images with better seeing conditions and lower background brightness should be given more weight. Put differently, images which have the lowest Poisson error should be given maximum weight. We use inverse error in size as weight when combining the σ_{xx}^2 , σ_{yy}^2 and σ_{xy}^2 of individual measurements. This was found to be optimal.

$$\sigma_{xx}^2 = \sum_i \sigma_{xx,i}^2 W(i) \quad (18)$$

where $\sigma_{xx,i}^2$ is the PSF corrected measurement in the i-th frame and the weight of the i-th image $W(i)$ is

$$W(i) = \frac{\epsilon_{\sigma_{xx,i}^2}^{-1}(true)}{\sum_{i=1} \epsilon_{\sigma_{xx,i}^2}^{-1}(true)} \quad (19)$$

where $\epsilon_{\sigma_{xx}^2(true)}$ is the error in $\sigma_{xx}^2(true)$. This is equivalent to $\epsilon_{\sigma_{xx}^2}$ and $\epsilon(xx)_{PSF}$ added in quadrature.

$$\epsilon_{\sigma_{xx,i}^2(true)} = \sqrt{\epsilon_{\sigma_{xx,i}^2}^2 + \epsilon^2(xx)_{PSF,i}} \quad (20)$$

Similar equation for σ_{yy}^2 and σ_{xy}^2 is used. After combining the individual measurements the error in final σ_{xx}^2 is

$$\epsilon_{\sigma_{xx}^2(true)} = \sqrt{\sum_{i=1} \epsilon_{\sigma_{xx,i}^2(true)}^2 W^2(i)} \quad (21)$$

Ellipticities e_1 and e_2 are calculated as

$$e_1 = \frac{\sigma_{xx}^2 - \sigma_{yy}^2}{\sigma_{xx}^2 + \sigma_{yy}^2} \quad (22)$$

$$e_2 = \frac{2\sigma_{xy}^2}{\sigma_{xx}^2 + \sigma_{yy}^2} \quad (23)$$

The error in the final ellipticity measurement can be calculated using standard error propagation equations. This comes out to

$$\epsilon_{e1}^2 = 4\epsilon_{\sigma_{xx}^2(true)}^2 \frac{\sigma_{xx}^4(true) + \sigma_{yy}^4(true)}{(\sigma_{xx}^2(true) + \sigma_{yy}^2(true))^4} \quad (24)$$

$$\epsilon_{e2}^2 = 8\epsilon_{\sigma_{xx}^2(true)}^2 \frac{\sigma_{xy}^4(true)}{(\sigma_{xx}^2(true) + \sigma_{yy}^2(true))^4} + 4\epsilon_{\sigma_{xy}^2(true)}^2 \frac{1}{(\sigma_{xx}^2(true) + \sigma_{yy}^2(true))^2} \quad (25)$$

In the above derivation we have assumed $\epsilon_{\sigma_{xx}^2(true)} = \epsilon_{\sigma_{yy}^2(true)}$. This is approximately true as long as the PSF and source is not extremely elliptical. Considering only a small fraction of the sources show extremely high ellipticity, this error equation is reasonably close to the true Poisson value.

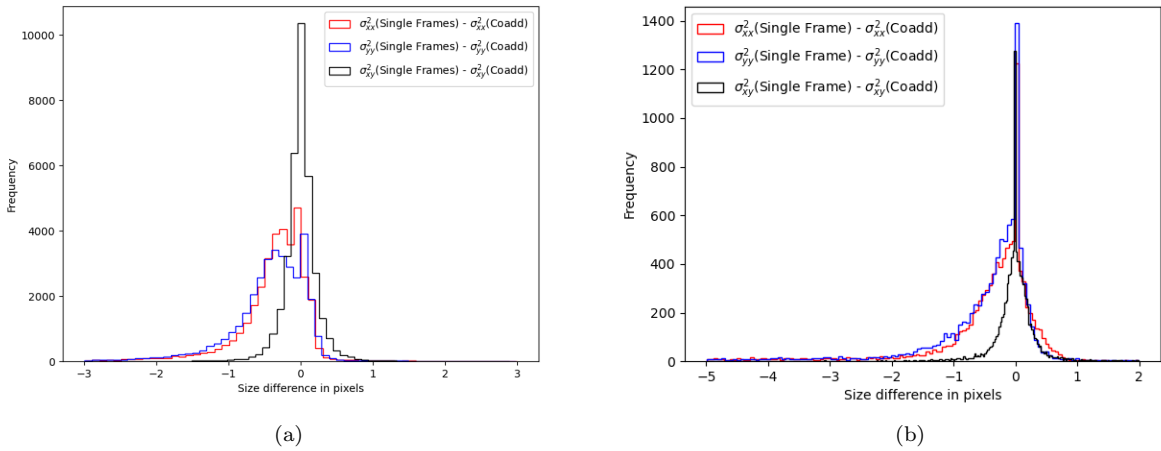


Figure 8. (a) Histograms for the difference in shape when sources are measured from the i+r co-add versus when they are measured in individual images of i and r band images. The individual image measurements are combined using inverse error as weight. The reduction in size by weighting individual frames optimally is clear from this plot. This leads to enhanced shear signal and hence shear recovery. (b) Histograms for the difference in shape when sources are measured from the weighted i+r co-add versus when they are measured in individual simulated images of i and r band images produced using PhoSim for the first case i.e. $\gamma_1 = 0.1$. The individual image measurements are combined using inverse error as weight. The reduction in size by weighting individual frames optimally is clear from this plot. This leads to enhanced shear signal and hence shear recovery.

On comparing the size measured from i+r co-added image to the the combined measurement from individual images we see a significant reduction in size for a large fraction of sources. This is shown in Figure 8a. A smaller size increases

the shear signal. In Figure 8b we show the same graph for simulated sources. The simulation is described in Section 3.

To recover shear from ellipticities, we adopt the method proposed in GREAT3 challenge (Mandelbaum et al. 2014)

$$g_t \approx \gamma_t = \frac{e_t}{2(1 - \langle e^2 \rangle)} \quad (26)$$

where γ_t is the tangential ellipticity, e_t is the tangential ellipticity of a source with respect to some given central point and $\langle e^2 \rangle$ is the average value of ellipticity squared. Reduced tangential shear is denoted by g_t . This equation was slightly modified to take into account the weight of each source.

$$g_t \approx \gamma_t = \frac{\sum_{i=1} e_{t,i} w_{a,i}}{2(1 - \langle e^2 \rangle)} \quad (27)$$

where $e_{t,i}$ is the tangential component of ellipticity of i-th source about a given point and the weight, $w_{a,i}$, the weight of the i-th source is defined as

$$w_{a,i} = \frac{\epsilon_{e,i}^{-2}}{\sum_{i=1} \epsilon_{e,i}^{-2}} \quad (28)$$

where ϵ_e is the error in ellipticity and

$$\epsilon_e^2 = \epsilon_{e1}^2 \frac{e_1^2}{e_1^2 + e_2^2} + \epsilon_{e2}^2 \frac{e_2^2}{e_1^2 + e_2^2} \quad (29)$$

where ϵ_{e1}^2 is error in e_1 and ϵ_{e2}^2 is error in e_2 . The tangential ellipticity, e_t , defined about a point can be written as

$$e_t = -e_1 \cos(2\phi) - e_2 \sin(2\phi) \quad (30)$$

where ϕ is the angle a line joining the point and the source makes and e_1 and e_2 are the ellipticity components. The cross component of ellipticity is similarly written as

$$e_c = -e_1 \sin(2\phi) + e_2 \cos(2\phi) \quad (31)$$

We also define

$$\langle e^2 \rangle = \sum_{i=1} e_i^2 w_{b,i} \quad (32)$$

The weights $w_{b,i}$ is defined as

$$w_{b,i} = \frac{\epsilon_{e,i}^{-1}}{\sum_{i=1} \epsilon_{e,i}^{-1}} \quad (33)$$

Using error propagation, the error in shear ϵ_γ^2 when using Equation 27 is

$$\epsilon_\gamma^2 = \gamma^2 \left[\frac{\sum_i w_{a,i}^2 \epsilon_{e,i}^2}{\left(\sum_i w_{a,i} e_{tan,i} \right)^2} + \frac{2 \sum_i w_{b,i}^2 \epsilon_{e,i}^2}{1 - \left(\frac{\sum_i e_i^2 w_{b,i}}{\sum_i w_{b,i}} \right)^2} \right] \quad (34)$$

where the summation is performed over all sources being considered, γ is the shear obtained, $\epsilon_{e,i}$ is the error in the ellipticity of the i-th sources, $e_{tan,i}$ is the tangential ellipticity component of the i-th sources and e_i^2 is the ellipticity of the i-th sources. The uncertainty in shear given by Equation 34 is entirely due to Poisson noise. However, when considering real-world data the error in shear is significantly worse due to systematic errors in telescopes, turbulence of the atmosphere, imperfection of CCD's, and a multitude of other effects. Single frame measurements will be affected the most since most of the sources are extremely faint in the individual images of a co-add. Hence, simulations are performed to understand these additional factors better.

3. VALIDATION

3.1. *Simulation and Co-add Measurements*

In order to test the ability of the pipeline described in Section 2 to recover shear accurately we test it on simulated images produced by PhoSim (Peterson et al. 2015, 2019, 2020, 2024). PhoSim is a ray tracing software that can simulate most of the known physics and hence produce extremely realistic images. We use the WIYN-ODI instrument which has been validated with real data from the telescope and simulate 30 images in i and r filter with 60s exposure time. The seeing and airmass were chosen at random from real i and r band images. We chose to simulate sources fainter than 17th magnitude to prevent saturation. We perform two sets of simulations in two different areas of the sky. This ensures we have different ensemble properties for the two cases. In the first case the galaxies in the PhoSim catalog were sheared by $\gamma_1 = 0.1$ and in the second case by $\gamma_1 = 0.05$. We pass the images through the exact co-add and detection method described above. The final co-add size is cropped to 10000x10000 pixels or 18.3'x18.3'. Source density in both cases is approximately 55 sources/arcminute². While on one hand, such a high number density from ground-based images is unlikely, on the other hand, it will help to test the performance in a crowded environment where blending issues pose a significant challenge for weak lensing analysis (Hartlap et al. 2011; Dawson et al. 2015).

For each image simulated, a 8 x 8 star grid is also simulated with the exact same seed which ensures all random parameters used in PhoSim are identical. This is done for two reasons. One, the clouds in each individual image is slightly different and hence the ZP will be slightly different. By simulating a star grid with stars of known magnitude we are able to calculate ZP accurately. Second, it helps us get an initial estimate of seeing and background. Our pipeline needs ZP, seeing, and background variance to create the weights for the co-add. The magnitude brightness of stars in this grid ranges from 16 to 23.

The simulated images were passed through the same pipeline as above. The PSF size of the i+r co-added image is 3.5 pixels and the error in σ_{xx}^2 , σ_{yy}^2 and σ_{xy}^2 is 0.18, 0.22 and 0.06 respectively. The size and errors are very similar for both sets of simulations since the same values of seeing, airmass, and seed were used for both. While the average size of the PSF is comparable to the real data, the errors are significantly smaller. The flux vs size graph is shown in Figure 5b. Points inside the red square are used for PSF estimation while the sources inside the black box are not used for weak lensing analysis to avoid shear dilution due to stars. The condition for the red box is $3.3 < \text{size} < 3.8$ pixels and $500 < \text{counts} < 10^5$. For the black box, the conditions are $2.5 < \text{size} < 4.5$ pixels and $10^2 < \text{counts} < 10^6$. These limits were obtained after careful visual examination. We also reject any sources larger than 12 pixels, which are likely due to severe cases of blending or sources brighter than 10^5 photon counts where brighter-fatter effect becomes important. This is clearly seen when considering the sources just above the red rectangle in Figure 5b. In total, the fraction of sources rejected by these cuts is roughly 1/3, most of them being stars enclosed by the black box in Figure 5b. This is in agreement with the PhoSim input catalog in which approximately 1/3 of all sources are stars. In Figure 7c and 7d we show histograms of star and galaxy size after PSF correction. The histogram of galaxy size shows a significant bump at 0.5 pixels which implies contamination from stars. This could potentially explain the slight underestimation of shear in Figure 9. The histogram of star size along with the best fit Gaussian in red is shown in Figure 6d, 6e, and 6f.

It was found a few percent of the sources with extremely small ellipticity errors, primarily large and bright sources, bias the shear measurement when using this scheme described in the previous section. Capping ellipticity error to 1/3 of the median ellipticity error values works well to recover shear and hence was adopted. Using this simple modification, we are accurately able to recover shear as shown in Figure 9. In this figure, we plot the shear measured as we start from a central circular region and increase the radius gradually to include more sources. The x-axis shows the radius of the circular region. On y-axis, we plot the recovered shear. We find the shear recovered from individual image measurements is more accurate than using shape measurements made in the co-add. In the second case, there seems to be a slight bias of ~ 0.005 . It was also found ϵ_e^2 i.e. the Poisson component of ellipticity error does not accurately predict error bars. This is expected since the simulations accurately take into effect most known physics while our error bars only take into account the Poisson statistics. We found 0.005 to be a more suitable error bar. This error bar also allows us to ignore the bias since it is comparable to the error bar. This error level is approximately 4 times the Poisson error calculated from the co-add and 10 times the error calculated from combined single frame measurements. These factors were adopted and applied to the Poisson error obtained from WIYN-ODI.

4. WEAK LENSING ANALYSIS

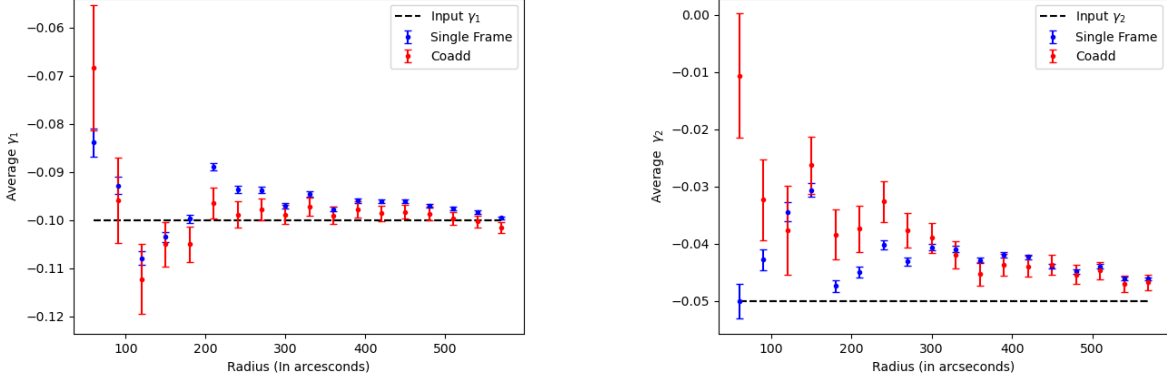


Figure 9. These plots show the ability of our pipeline to accurately recover shear at various levels in the weak lensing regime. To make these plots, we give PhoSim simulations input shear of $\gamma_1 = 0.1$ in the first case and $\gamma_2 = 0.05$ for the second case. It is clear both co-add and individual frame measurements accurately recover shear to within 0.005 of the true shear. In the second case, there is slight bias of approximately 0.005. The error bars shown are just the Poisson component. Clearly, single frames have smaller error bars as expected. However, the error bars fall short because of non-Poisson sources of error. Hence we elect to use error bars of 0.005 for shear measured using individual image measurements which is approximately 10 times the Poisson component.

4.1. Aperture Mass Maps

A common method of detecting mass concentrations using weak lensing is aperture mass statistics (Kaiser 1995; Schneider 1996; Gruen et al. 2013). It measures the average tangential orientation of background galaxies around some point convolved with a weight. Aperture mass M_{ap} and the associated error $\sigma_{M_{ap}}$ are defined as

$$M_{ap} = \sum_i w(|\theta| - |\theta_i|) w_p(i) g_{i,t} \quad (35)$$

$$\sigma_{M_{ap}} = \sqrt{\sum_i w^2(|\theta| - |\theta_i|) w_p(i)} \quad (36)$$

where $g_{i,t}$ is the tangential alignment of the i -th galaxy and $w_p(i)$ is the weight function derived from Poisson error in ellipticity, and the overall weight function is denoted by $w(|\theta|)$. θ represents the generalized co-ordinates. Specifically the weight due to inverse Poisson error in ellipticity is

$$w_p(i) = \frac{1}{\epsilon_e^2(i)} \quad (37)$$

Several different weight schemes can be found in literature (Schneider 1996; Schirmer et al. 2004; Gruen et al. 2013). We use Gaussian weight (Gruen et al. 2013) for simplicity.

$$w(|\theta|) = \begin{cases} \exp(-|\theta|^2/2\sigma_w^2) & \text{when } |\theta| < 3\sigma_w \\ 0 & \text{when } |\theta| > 3\sigma_w \text{ or } |\theta| < 50 \text{ pixels} \end{cases} \quad (38)$$

where σ_w is the width of the weight function. The size of σ_w is usually a few arcminutes. A smaller value brings out details at a finer spatial scale but at the cost of more noise. This is because, for a smaller width, averaging of shear is done in a smaller area using a small number of background galaxies. A larger value of width washes out details of mass distribution but has a lower noise.

For Poisson error in ellipticity ϵ_e , we apply the error cap at 1/3 the median error value in order to prevent the measurements from being dominated by bright sources with extremely low errors. The significance maps is then defined as $M_{ap}/\sigma_{M_{ap}}$. M_{ap} is also called the Aperture Mass maps or E-mode maps. To make the B-mode maps the tangential component of shear is replaced by the cross component. In other words, we simply replace g_t with g_c in Equation 35. This is defined as

$$g_c \approx \gamma_c = \frac{\epsilon_e}{2(1 - \langle e^2 \rangle)} \quad (39)$$

A major issue in making the aperture mass maps is that source density varies significantly over a large field. In our case, the source density varies by a factor of 2 in the $40' \times 43'$ field of view. This produces mass maps that have different error levels in different regions of the image. The problem gets particularly worse at the edges. Hence, we decide to use an adaptive weight scheme. Simply put, we change σ_w depending on the source density. The width is smaller in regions of high source density and conversely, the width is larger when the source density is smaller. The width is changed to get σ_{Map} varying by at most 10% throughout the field, except at the edges. However, we limit the maximum width to 3000 pixels and the minimum width to 500 pixels. The maximum value of width is reached only at the edges.

In Figure 10 we show the comparison of the aperture mass map with the light density maps in the central part of the cluster. To make the light density maps we select all galaxies with photometric redshift between 0.15 to 0.55 where the reliability parameter of EAZY is greater than 0.8. We also reject galaxies where the source was measured in less than 3 bands. This range includes the galaxy cluster Abell 2390 which has been spectroscopically confirmed at $z=0.23$ (Abraham et al. 1996). We reject any galaxy with size greater than 10 pixels. Then we divide our images into grids of 50×50 pixels. For each grid position, we calculate the light from the galaxies in a $5.5'$ radius and weigh them by a Gaussian of width $0.73'$. The adaptive E-Mode maps are made by fixing the value of σ_{Map} within the range $3.5 \times 10^{-4} \pm 1.75 \times 10^{-5}$ and considering the galaxies in the redshift range $z = 0.4$ to 2.0 . We do not consider galaxies with $z > 2.0$ since in this range a large fraction of the sources represent catastrophic failure of the photo- z code. Once again we only consider galaxies where the reliability score of photometric redshift is greater than 0.8 and flux information is available in at least 3 filters. We also reject sources larger than 10 pixels in size or sources where the bkgflag is raised. These conditions are not mutually exclusive and there is significant overlap. Changing the conditions slightly does not significantly affect our results. The main peak of the E-mode maps line up extremely well with the galaxy density maps which in turn lines up with the central cD galaxy and X-Ray maps Allen et al. (2001). In Figure 11a we show the contours of the Aperture Mass Map overlaid on the light density map of galaxies in the redshift range $z = 0.15$ to 0.55 . The symbols show the location of galaxy clusters and groups obtained from the NASA Extragalactic Database. Figure 12 shows the light density map of galaxies in the redshift range $z = 0.35$ to 0.75 with contours of Aperture Mass Map overlaid on it. We discuss these maps in detail in Section 6.

4.2. Mass Maps

Aperture mass maps are useful for locating peaks and the general structure of mass distribution. However, one of the key objectives of weak lensing studies are measurement of mass. We follow the method of Kaiser & Squires (1993) which was later generalized by Seitz & Schneider (1995) to estimate the mass. $\kappa(\theta)$ is given as

$$\kappa(\theta) \approx \frac{1}{2\pi\bar{n}} \sum_{n=1}^N \frac{W(\theta - \theta_n, s)\gamma_{n,t}}{\theta_n^2} \quad (40)$$

where $\gamma_{n,t}$ is the tangential shear of the n -th source, \bar{n} is the density of sources and

$$W(x, s) = 1 - \left(1 + \frac{x^2}{2s^2}\right) \exp\left(-\frac{x^2}{2s^2}\right) \quad (41)$$

where x is the distance of the source from the point about which we calculate $\kappa(\theta)$ and s is the window width. The weight function $W(x)$ in effect suppresses noise at a small radius. If a very small window function is chosen then the image becomes extremely noisy. On the other hand, if a large value of s is chosen then the details of mass distribution are washed out. It was found that $s = 200$ pixels or $22''$ produces optimal result. To produce the κ map the exact same procedure used to make E-Mode maps is followed, except we now no longer use adaptive values. We also only consider galaxies in a radius of $7.33'$ for any given point. The map of $\kappa(\theta)$ for the entire field is shown in Figure 11b. The error level in each pixel was determined using error propagation and multiplying the resulting Poisson error with a factor of 10 to take into account systematic/non-Poisson sources of error, as determined from PhoSim simulations. To convert from $\kappa(\theta)$ to enclosed mass we use

$$\kappa(\theta) = \frac{\Sigma}{\Sigma_{crit}} \quad (42)$$

where Σ is the mass enclosed and

$$\Sigma_{crit} = \frac{c^2}{4\pi G} \frac{D_s}{D_l D_{ls}} \quad (43)$$

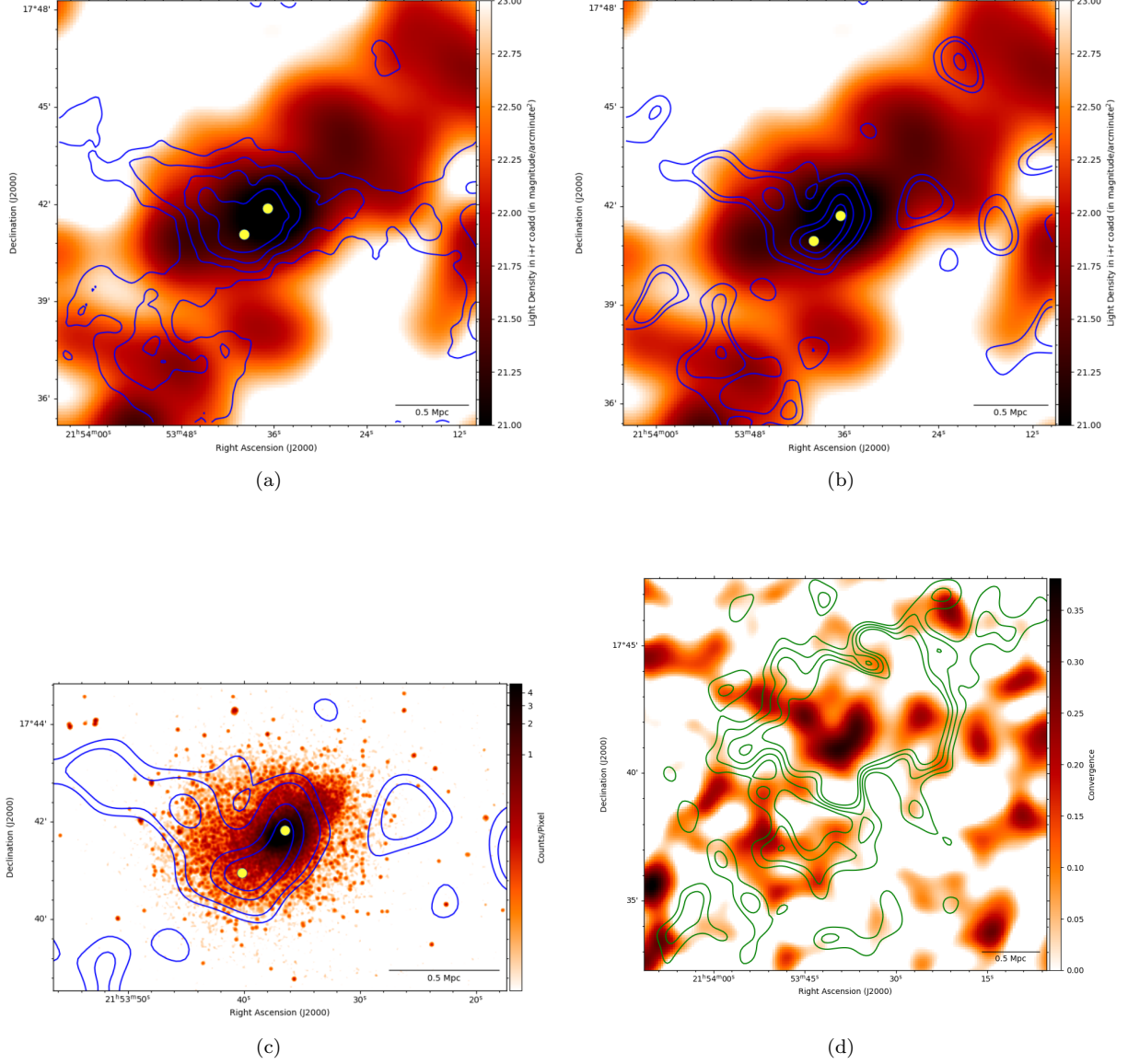


Figure 10. (a) The contours of E-Mode (i.e. M_{ap}) maps shown in blue are overlaid on the galaxy light density maps. Contours are drawn at 0.012, 0.024, 0.036 and 0.048. The light density maps are made by adding light from galaxies in the range $z = 0.15$ to 0.55 weighted by a Gaussian of width $0.73'$. The main peak matches up perfectly. The smaller peak on the lower left is distinctly separate from the E-Mode peak. The two peaks of the E-Mode map are shown as yellow circles (b) Same as before except the contours are from the convergence map. Contours are drawn at 0.1, 0.15, 0.25 and 0.3. The two peaks of the convergence map are shown as yellow circles (c) In color shown is the X-ray image from Chandra with the convergence map contours overlaid. A slight swirl pattern in the X-Ray can be seen matching the swirl pattern of the convergence contours. (d) The convergence map is shown as background. Contours show the compact component subtracted radio images from LOFAR obtained after careful re-analysis of DR2 data by Cianfaglione et al (in prep). Contours are drawn at 0.0014, 0.0021, 0.0028, 0.0035 Jy/beam which corresponds to 2, 3, 4 and 5σ significance respectively

Where D_s is the angular distance to the source, D_l is the angular distance to the lens, and D_{ls} is the angular distance measured by an observer at the location of the lens to the source. This is not the same as simply subtracting D_s and D_l and depends on the curvature of the universe. It should be noted that Σ_{crit} is defined for a single source. However, in weak lensing analysis, one typically has thousands of background sources at various redshifts for a given lens system. In our case, the lens system is Abell 2390. Hence an average value of $\frac{D_s}{D_{ls}}$ is determined to find Σ_{crit} .

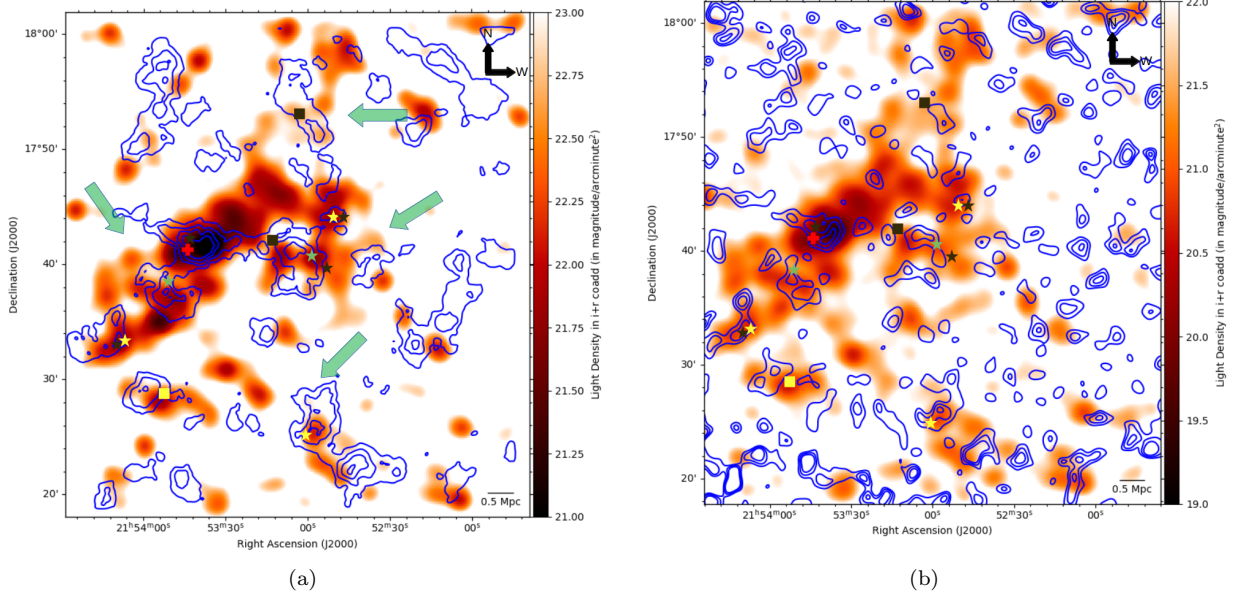


Figure 11. (a) The contours show the E-Mode (i.e. M_{ap}) maps constructed from the galaxy sample in the range $z=0.4$ to 2.0 overlaid on light density map of galaxies in redshift range $0.15 - 0.55$. We fixed $\sigma_{M_{ap}} = 3.5 \times 10^{-4} \pm 1.75 \times 10^{-5}$. Contours are drawn at levels $0.012, 0.024, 0.036$ and 0.048 . The background is light density map that was smoothed with a Gaussian width of $0.73'$. Four major filamentary structures connecting the galaxy cluster are visible and are shown in green arrows. One to the north, one to the west (right), and one towards the southwest (down right). Another structure to the southeast is also visible. The filament seen from the contours broadly agrees with the filaments seen in the light density maps. The location clusters obtained from NED are shown as symbols. The squares are obtained from X-ray studies while the stars are obtained from optical data. Cross symbols show cluster location obtained using the SZ effect on Planck data. Each symbol and the corresponding literature is discussed in detail in Section 6. (b) Contours of $\kappa(\theta)$ is overlaid on the light density maps smoothed with a Gaussian of $0.73'$ of galaxies in the range $z = 0.15$ to 0.55 . Contours have been drawn at levels $0.1, 0.2$ and 0.3 . The $\kappa(\theta)$ map has been smoothed with a Gaussian of width $16.5''$. The bimodal mass distribution of the central region of Abell 2390 can be clearly seen at R.A = $21^{\text{h}}:53^{\text{m}}:36.8\text{s}$ and Dec = $17^{\circ}:41':43''$. The other peaks are consistent with the mass concentrations shown by E-Mode maps. We find also increased noise at the edges of $\kappa(\theta)$ map.

The average value is defined as (Okabe et al. 2010)

$$\left\langle \frac{D_s}{D_{ls}} \right\rangle = \int \frac{D_s}{D_{ls}} \frac{dp}{dz} dz \quad (44)$$

where dp/dz is the redshift probability distribution of source galaxies used for weak lensing measurements. We use the redshift value obtained using EAZY photo-z as described in Section 2.4. In our case, this value comes out to 0.66 . This leads to a Σ_{crit} value of $4.23 \times 10^{15} M_{\odot}/\text{Mpc}^2$ which is in agreement with the value of $4.55 \times 10^{15} M_{\odot}/\text{Mpc}^2$ obtained by Squires et al. (1996). Our value for $\langle D_s/D_{ls} \rangle$ is in agreement with the value of 0.69 obtained by Okabe et al. (2010) with images comparable depth to ours. This is remarkable since both Squires et al. (1996) and Okabe et al. (2010) were unable to perform photo-z due to lack of color information. A comparison of mass enclosed in the inner part of Abell 2390 with Squires et al. (1996) is shown in Figure 13. We find an excellent match up to a radius of 0.7 Mpc from the cluster center. The mismatch after that is likely due to mass sheet degeneracy which states that $\kappa(\theta)$ can be approximately determined to an additive constant. For a detailed discussion on mass sheet degeneracy see Bradač et al. (2004).

4.3. 3-D Slices

The ability to make slices of mass distribution at various redshifts would be the ultimate test of any deep weak lensing analysis. One of the first maps 3-D weak lensing reconstruction was done by Massey et al. (2007). It used high-quality images obtained from HST to measure shear in each redshift bin. However, such reconstructions are extremely rare in literature, especially with ground-based data. One of the challenges in making such a 3-D map is

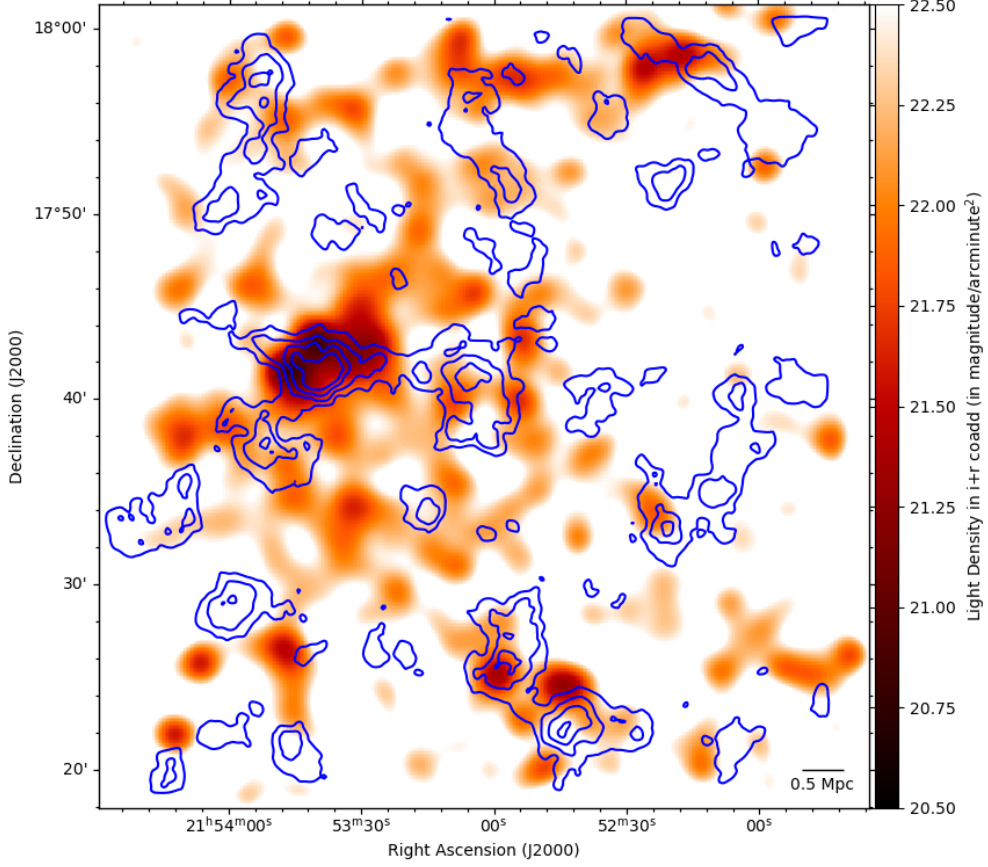


Figure 12. The contours show the E-Mode (i.e. M_{ap}) maps constructed from the galaxy sample in the range $z=0.4$ to 2.0 overlaid on light density map from galaxies in the redshift range 0.35 to 0.75 . Contours are drawn at levels 0.012 , 0.024 , 0.036 and 0.048 . We fixed $\sigma_{M_{ap}} = 3.5 \times 10^{-4} \pm 1.75 \times 10^{-5}$. The background is light density map that was smoothed with a Gaussian width of $0.73'$.

galaxy density. In weak lensing one typically requires a few tens of galaxies arcminute^{-2} to measure shear. However, when these are divided into redshift bins, the galaxy density is drastically decreased which introduces more noise. Below we describe our approach.

We construct an E-Mode map, E_1 with all galaxies in the redshift range $z=0.01$ to 2.0 . We only consider the sources that satisfy the conditions mentioned in Section 4.1. This map, in an ideal case, traces most cosmic structures from $z=0$ to 2.0 . We construct a second E-Mode map, E_2 with all galaxies in the range $z=0.5$ to 2.0 . This E-Mode map boosts the structures in the range $z=0.01$ to 0.5 since it only contains galaxies background to $z=0.5$. This can be written down as

$$E_1 = S_1 \left(\frac{N_2}{N_1 + N_2} \right) + S_2 \quad (45)$$

$$E_2 = S_1 + S_2 \quad (46)$$

where S_1 is the cosmic structure in the foreground slice and S_2 is the structure in the background slice. N_1 is the number of sources in redshift range $z=0.01$ to 0.5 i.e. the foreground slice and N_2 is the number of sources in redshift range $z=0.5$ to 2.0 i.e. background slice. The factor $\left(\frac{N_2}{N_1 + N_2} \right)$ signifies that only the population N_2 trace structure S_1 .

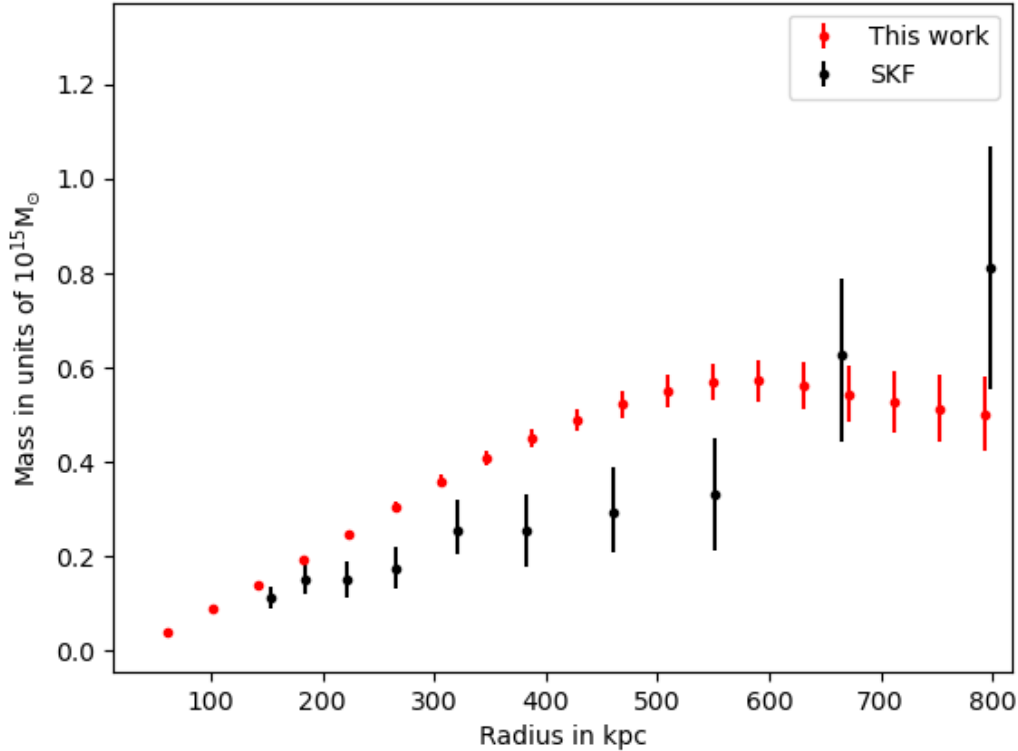


Figure 13. Enclosed mass as a function of radius from the center of the galaxy cluster. The center is located on the BCG at R.A = 21h:53m:36.8s and Dec = 17°:41′:43″. We used Poisson error bars and multiplied them with a factor of 10, as found in PhoSim simulations, to take into account systematic/non-Poisson errors. We find our data matches extremely well Squires et al. (1996) up to radius of 700 kpc. The mismatch beyond that is likely due to mass sheet degeneracy and can be remedied using a small additive constant.

It was found significant noise arises from the fact that the resolution of E-mode maps are different, with E_1 having significantly better resolution than E_2 . This is because the number of galaxies used to construct E_2 is approximately half of the number of galaxies used to construct E_1 . To remedy this we bring all E-Mode maps to the same resolution. We smooth E_1 by a Gaussian of width 4 pixels i.e. $22''$ and E_2 by a Gaussian of width 2 pixels i.e. $11''$. This was visually determined after careful examination of the two E-Mode images i.e. E_1 and E_2 .

While in theory all pixels of the E-Mode maps matter, we note that in reality, the shear signals are extremely small. Hence only the brightest few pixels in the E-Mode image contain information. It was found that capping the minimum value of E-mode maps at 1 standard deviation from the media of all pixels in the image produces better results. This value in our case comes out to approximately 0.014 for E_1 and 0.018 for E_2 . The E-Mode maps were produced in an adaptive manner constraining $\sigma_{M_{ap}} = 4.5 \times 10^{-4} \pm 2.25 \times 10^{-5}$. Next, using inversion of Equations 45 and 46 mentioned above we recovered the two slices. The E-Mode contours of both the foreground and background slice are shown in Figure 14 We find the foreground slice contains signal from Abell 2390 while the background slice is completely devoid of signal from Abell 2390. A few of the more prominent sub-structures can be seen in the foreground slice. The background slice is very noisy and the contours do not seem well correlated to light density maps. This is not surprising since after all the cuts mentioned above, E_2 had an extremely low source density of 8 galaxies/arcmin⁻².

5. DISCUSSION

Abell 2390 has been extensively studied in X-Ray (Pierre et al. 1996; Allen et al. 2001; Martino et al. 2014; Sonkamble et al. 2015), optical (Abraham et al. 1996; Hutchings et al. 2002), radio (Bacchi et al. 2003; Augusto et al. 2006; Sommer et al. 2016; Savini, F. et al. 2019), weak lensing (Squires et al. 1996; Umetsu et al. 2009; Okabe et al. 2010;

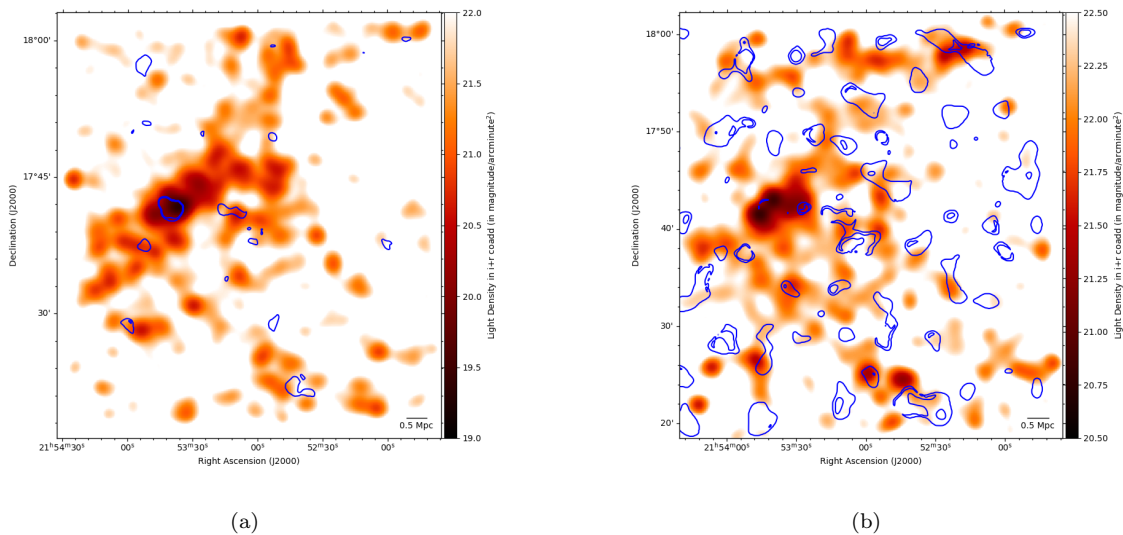


Figure 14. (a) The adaptive E-Mode contours from the foreground slice ($z = 0.01$ to 0.6) overlaid on an image showing the light density of galaxies in the redshift range $z = 0.15$ to 0.55 smoothed by a Gaussian of width $0.73'$. (b) The contours depicted are from the adaptive E-Mode maps of the background slice ($z = 0.5$ to 2) overlaid on an image showing the light density of galaxies in the redshift range $z = 0.35$ to 0.75 similarly smoothed. In both cases, contours are placed at levels of 0.02 , 0.07 , and 0.12 . There is significant noise in our maps. The signal from Abell 2390 appears only in the foreground slice as expected.

von der Linden et al. 2014) and strong lensing (Narasimha & Chitre 1993). The central continuum source of the BCG shows young, compact, and self-absorbed jets (Edge et al. 1999; Augusto et al. 2006). Accretion towards the central supermassive black hole has also been inferred from CO, CN, SiO, HCN and HCO+ absorption lines against the radio continuum source, which show molecular gas clouds moving in toward the galaxy center at roughly 100 to 300 km/s (Rose et al. 2019, 2024b). In Figure 15 we show a composite image of X-ray (in red), the convergence map (in blue) overlaid on the optical image of Abell 2390. In the following sections, we briefly discuss these previous findings and compare them to our results.

5.1. X-Ray

High-resolution X-ray images of Abell 2390 were obtained and analyzed by Allen et al. (2001). ROSAT data for this cluster has been analyzed by Pierre et al. (1996). However, the Chandra data is much more detailed and hence we focus on that. Allen et al. (2001) found that the X-ray profile can be fit well to a NFW profile. A variety of other profiles such as softened isothermal sphere and full isothermal sphere were also found to provide reasonably good fits. They also note that this cluster does not seem to be completely relaxed. Both Allen et al. (2001) and Rose et al. (2024a), find evidence of excess X-ray emission approximately $5''$ South-East of the central peak, which coincides with the BCG. We note here that this excess was found using two independent methods. Allen et al. (2001) used adaptive smoothing to find the excess, while Rose et al. (2024a) subtracted a double beta model. Both methods show the excess emission is approximately 20 kpc ($5''$) from the central peak. It is hypothesized by Allen et al. (2001) that the cluster has not fully relaxed from the last merger. The model subtracted images of Rose et al. (2024a) are interesting because they seem to show two cores orbiting one another (their figure 6). However, there is a chance the excesses and depressions seen in the model subtracted images are a result of AGN activity. Indeed this has been suggested by Sonkamble et al. (2015). Evidence of current AGN activity at kpc scale was found by Augusto et al. (2006), with moderate high radio frequency variability of the radio continuum since 2015 also identified by Rose et al. (2022).

5.2. Radio Observations

It has been known for decades that massive merging clusters are likely to host radio emission in the form of radio halos and radio relics (van Weeren et al. 2019). The synchrotron radio emission would be caused by the re-acceleration of cosmic ray electrons by turbulent motions that develop in the ICM during cluster mergers.

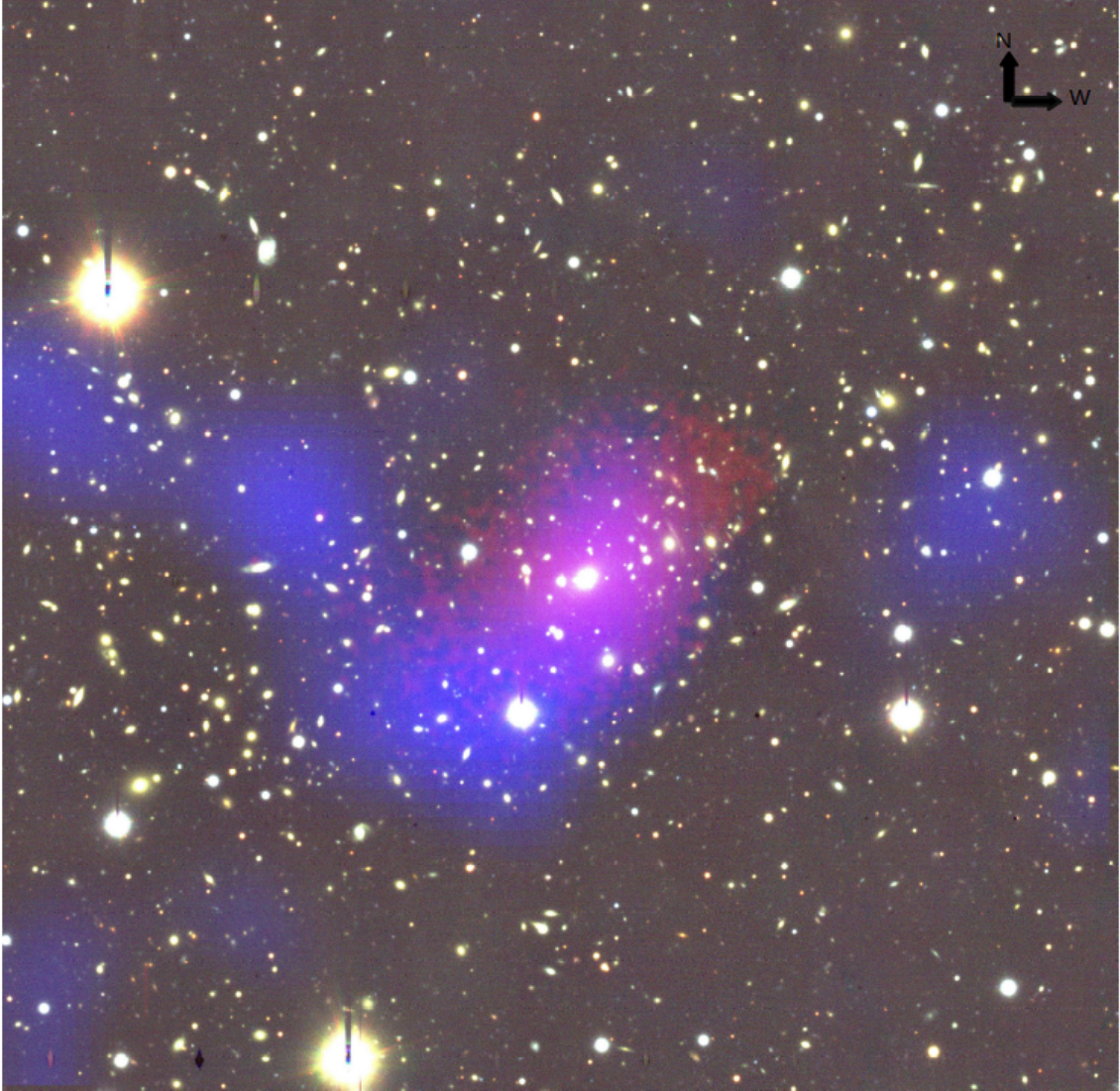


Figure 15. A composite image of Abell 2390. The X-ray obtained using Chandra (Allen et al. 2001) is shown in red and our mass map (convergence) in blue. It is overlaid on the RGB color image of Abell 2390 created using g band coadd for blue, r band coadd for green and i band coadd for red. Optical images have been obtained using WIYN-ODI. At the center of the image, the bright elliptical galaxy is the BCG. The X-Ray shows a swirl-like pattern in the same direction as the DM.

In the past years, radio observations have started to reveal radio halos in clusters that are not undergoing major mergers, and that – in some cases – host a cool core (e.g. Bonafede et al. (2014); Sommer et al. (2016); Venturi et al. (2017); Savini, F. et al. (2019); Biava et al. (2024)). These results indicate that these sources might be connected to the occurrence of minor/off-axis mergers, though it remains unclear how minor mergers could initiate continuum emission on megaparsec scales.

Abell 2390 is one of these clusters, as it hosts both a cool core and signs of minor dynamical disturbances from the X-ray morphological parameters. Diffuse radio emission in Abell 2390 was first discovered and classified as a radio mini halo by Bacchi et al. (2003) and then as a radio halo by Sommer et al. (2016). LOFAR observations revealed the presence of a double radio galaxy with the lobes extending in the east-west axis for ~ 600 kpc, and Savini, F. et al. (2019) could not distinguish the radio emission from the radio galaxy from a possible contribution from the radio halo, leaving the possibility of a radio halo open. Savini, F. et al. (2019) also noted that radio galaxies of such a size are uncommon at the center of galaxy clusters, as the ICM prevents the expansion of the lobes to such large scales.

LOFAR observations of Abell 2390 have also been published in the LOFAR Data Release 2 (Botteon et al. 2022), and the authors concluded that most of the emission came from the radio galaxy.

Cianfaglione et al (Master thesis, in prep) have re-analyzed the data from the LOFAR DR2, and subtracted the central AGN using an approach tuned “ad-hoc” for this cluster. Specifically, they subtracted all the emission on scales smaller than $375''$, corresponding to 1390 kpc, and re-imaged the data at low resolution (that is $1'$) to gain sensitivity towards the extended emission (Figure 10d). They found residual radio emission with a flux density $S(144 \text{ MHz}) = 0.16 \pm 0.03$ Jy, corresponding to a monochromatic power $P(144 \text{ MHz}) = 2.7 \pm 0.5 \times 10^{25}$ W/Hz. In addition, the emission radial profile follows the exponential profile typically found in radio halos. The radio halo emission extends for 1450 kpc. As the size, power, and radio profile are all in line with those of radio halos in clusters of similar mass (Cuciti et al. 2023), they concluded that the residual emission is actually a radio halo. The presence of a radio halo reinforces the results obtained in this work, as they are in line with the presence of dynamical activity. If the merger is indeed in a late stage, as derived in this work, we expect the radio halo emission to be steep (Brunetti & Jones 2014; Savini, F. et al. 2019; Biava et al. 2024). Sommer et al. (2016) using VLA data estimates the overall spectral index to be 1.6 which is fairly high.

High-resolution radio images of the BCG using ALMA to detect CO reveal an extended tail Rose et al. (2024a). They considered various scenarios, including both outflows and inflows, and came to the conclusion that a recent gravitational disturbance of the central BCG is the most likely explanation of the extended tail. Alcorn et al. (2023) using CFHT/SITELLE finds the BCG has a tail matching the findings of Rose et al. (2024a). All of this points to a fairly disturbed structure in the central region.

5.3. *Lensing and Spectroscopy*

Abraham et al. (1996) made spectroscopic measurements of this galaxy cluster using Canada-France-Hawaii Telescope (CFHT). They found spectroscopic evidence of an in-falling galaxy stream from the NW corner approximately $10'$ from the center of A2390. This can also be seen from the light density maps shown in Figure 11a. This group of galaxies has also been identified using optical cluster finding algorithms, shown as yellow and black stars in Figure 11a.

A strong lensing study of this cluster was performed by Narasimha & Chitre (1993). Weak lensing studies have also been conducted using data obtained from CFHT Telescope (Squires et al. 1996) Subrau Telescope (Umetsu et al. 2009; Okabe et al. 2010). It was also studied by von der Linden et al. (2014) by using data from both telescopes. These studies, except for von der Linden et al. (2014) do not find evidence of a merger in the galaxy cluster using weak lensing maps. However, we note here that the only two studies with depth comparable to ours are Okabe et al. (2010) and von der Linden et al. (2014). We also note von der Linden et al. (2014) come to the conclusion that evidence of merger activity from the North-West, presumably the same galaxy group discovered by Abraham et al. (1996), is present in this cluster. While our light maps in Figure 11a clearly show this, we are not able to recover this with very high confidence. We detect the peak of this smaller group with somewhat lower confidence. We believe this is a minor and early-stage merger event. In addition to this, we also find evidence of gravitational disturbance in the central region of Abell 2390. Our convergence maps show the DM cores are in the process of merger. Aperture mass maps of von der Linden et al. (2014) look similar to ours, in the sense that they find a bimodal mass distribution at the core. Due to the significantly worse resolution of their map, unfortunately, any further comparison is difficult.

5.4. *Late Merger Hypothesis*

We believe Abell 2390 is a case of extreme late-stage merger as suggested by Allen et al. (2001). It seems to be the most likely explanation of all observed data. During this merger, the hot gas experienced friction when orbiting the cluster while the DM component experienced very little of this friction, if any. This caused the hot gas to lose angular momentum and fall into the central core faster than the DM. Currently, the hot gas is almost merged with the central core since it can only be detected using adaptive smoothing (Allen et al. 2001) or model subtraction (Rose et al. 2024a). The DM core still shows signs of an ongoing merger. In our mass maps, the mass excess is found southeast of the main peak at a separation of approximately $1'$ or 220 kpc. This separation, while in the exact same direction as the X-ray excess, is about 10 times more when compared to the X-ray separation of $5''$ i.e. 20kpc. A slight swirl pattern in the lower left of the X-ray image in Figure 10c is visible and matches up with the swirl seen on the overlaid convergence contours lending support to this hypothesis.

The late-stage merger would cause gravitational disturbance primarily in the central regions of the cluster. This is supported by the extended tail of the BCG found by Rose et al. (2024a). The direction of the tail also matches with

the expected direction from a late-stage merger. The process of an ongoing merger from the southeast would cause the plume in the BCG to be in the northwest direction.

The extended radio emission found by Sommer et al. (2016) and Cianfaglione et al. also supports our hypothesis. The late-stage orbital motion of two heavy DM cores will introduce significant turbulence and ripples in the ICM which leads to the re-energizing of leptons, which in turn leads to a radio halo with a steep spectral index. Sommer et al. (2016) estimated the spectral index to 1.6 which is very steep and consistent with our hypothesis of a late-stage merger.

6. SMALLER GROUPS AND LARGE SCALE STRUCTURE

Weak lensing provides one of the most powerful ways to map large-scale structures of Dark Matter through the Universe (Refregier 2003). This is especially useful in probing regions of lower density such as filamentary structures and smaller galaxy groups since shear depends linearly on mass enclosed. Other methods such as X-rays are ineffective in studying these regions since X-ray brightness depends on density squared (Ettori 2000). Hence X-ray signals from low-density regions cannot be detected. These regions are difficult to detect in Radio wavelengths as well due to lower concentrations of ICM and ultra-relativistic particles in the ICM. Reliable detection of these lower mass structures can be used in conjunction with mass, redshift, and distribution of larger structures, such as galaxy clusters, to better constrain cosmological models (Bernardeau et al. 1997; Jain & Seljak 1997).

In Figure 11a we show the light density of the $i+r$ co-add as the background color. We only consider galaxies in the redshift range $z = 0.15$ to 0.55 and the galaxies that pass all the size, flag, and flux cuts mentioned in Section 4.1. This is the baryonic mass distribution and is roughly expected to follow the large-scale structure. The contours from the aperture mass map are overlaid on this. The symbols show the reported galaxy groups and clusters on NED (NASA Extragalactic Database). The star symbols were obtained using cluster-finding methods that rely on optical data. The yellow star corresponds to the list published by Wen et al. (2012) and later updated by Wen & Han (2015). The black star corresponds to the list published by Rozo et al. (2015). Both of these methods primarily use SDSS data. The green star corresponds to the list published by Gal et al. (2009) using data from the Digitized Second Palomar Observatory Sky Survey. X-ray analysis of this region of the sky is primarily based on XMM-Newton data. The location of smaller groups and clusters based on available X-Ray data is shown in squares. The black square shows the location of groups mentioned in Haines et al. (2018). The yellow square corresponds to locations mentioned in Giles et al. (2022). The red cross is cluster location derived from the SZ effect in Planck data (Ade et al. 2016; Khatri 2016). It is clear in Figure 11a that most of the smaller galaxy groups are successfully detected by our aperture mass map. There are some regions in our map that have high light density but is neither detected by weak lensing nor the different galaxy group detection methods mentioned above. This could arise from a variety of factors. The light maps could be contaminated with light from sources that are not within the desired redshift range. It could also be the case that our images are significantly deeper than any existing data to which the cluster-finding algorithms have been applied. Thus, these structures are visible in our light map only.

It has been shown that aperture mass statistics or significance maps are able to trace the cosmic filamentary structures (Jauzac et al. 2012; HyeonHan et al. 2023). We are able to recover a few broad filamentary structures as shown in Figure 11a. We notice 4 major structures in the light density maps. One towards the north, one to the west, one to the southwest, and one to the southeast. All of these are broadly traced by the contours. The contours also trace a structure to the northeast where there seems to be a small galaxy group. We note that neither the aperture mass map nor the convergence map is able to detect the filament northwest of the central region. In Figure 12 we overlay the E-Mode contours on light density maps of galaxies in the redshift range $z = 0.35$ and 0.75 . The light density maps are made using the same method as before.

7. CONCLUSION

In this paper we present a weak lensing analysis of the galaxy cluster Abell 2390 using extremely deep images obtained from WIYN-ODI. We introduce a novel method that allows us to obtain shear information from galaxies which are measured to be smaller than the PSF. This allows us to create mass maps with higher source density than previously possible with images of similar depth. We measured shapes in individual exposures using a moment matching algorithm. The forced measurement method was used when SNR was too low for convergence. The aperture mass maps obtained show that we are able to recover most of the smaller galaxy groups, identified using optical and X-ray cluster-finding algorithms. A group of galaxies approximately $10'$ North-West of the cluster was also found and

appears to be in the process of infalling into the cluster from spectroscopic data. In addition to this, most of the filamentary structures around Abell 2390 were also recovered in the aperture mass maps. Within a radius of ~ 220 kpc from the BCG, Abell 2390 appears to have a bi-modal mass distribution, with the smaller peak being southeast of the main peak, which is consistent with the X-ray excess found in Chandra data. The separation between the peaks is 220 kpc whereas the separation in X-Ray is 20 kpc. This suggests that Abell 2390 is a case of an extreme late-stage merger, with the hot gas close to the center now being completely relaxed following the most recent merger. However, due to the lack of friction during the infall period, the dark matter is still actively merging with the main DM core. The merger hypothesis is supported by CO radio observation using ALMA which find a tail in the BCG that can be explained by a recent gravitational disturbance. The high spectral index of 1.6 found using VLA data and radio halo found in both VLA and careful re-examination of LOFAR DR2 also support this hypothesis. If true, more such findings in other galaxy clusters along with simulations might help us put upper limits on the cross-section of DM. We find our mass estimate for this galaxy cluster is consistent with previously published results.

8. ACKNOWLEDGMENTS

The authors thank the anonymous referee for the useful comments and suggestions. The authors would like to thank Purdue University for its continued support. We are also very grateful to the WIYN-ODI PPA team, especially Wilson Liu, Nick Smith, Arvind Gopu and all the telescope operators for their help in obtaining excellent quality data. We also thank the Purdue Rosen Center for Advanced Computing (RCAC) for access to computing facilities that have been extensively used in this paper. This data analysis has been done on python and the authors acknowledge the use of astropy (Astropy Collaboration et al. 2013b, 2018, 2022), numpy (Harris et al. 2020), scipy (Virtanen et al. 2020), matplotlib (Hunter 2007) and aplpy (Robitaille & Bressert 2012; Robitaille 2019). This research has made use of the NASA/IPAC Extragalactic Database (NED), which is funded by the National Aeronautics and Space Administration and operated by the California Institute of Technology.

Facilities: WIYN-ODI 3.5m,

REFERENCES

- Abraham, R. G., Smecker-Hane, T. A., Hutchings, J. B., et al. 1996, *The Astrophysical Journal*, 471, 694–719, doi: [10.1086/177999](https://doi.org/10.1086/177999)
- Ade, P. A. R., Aghanim, N., Arnaud, M., et al. 2016, *Astronomy and Astrophysics*, 594, A27, doi: [10.1051/0004-6361/201525823](https://doi.org/10.1051/0004-6361/201525823)
- Alcorn, L. Y., Yee, H. K. C., Drissen, L., et al. 2023, *MNRAS*, 522, 1521, doi: [10.1093/mnras/stad948](https://doi.org/10.1093/mnras/stad948)
- Allen, S., Ettori, S., & Fabian, A. 2001, *Monthly Notices of the Royal Astronomical Society*, 324, 877–890, doi: [10.1046/j.1365-8711.2001.04318.x](https://doi.org/10.1046/j.1365-8711.2001.04318.x)
- Annis, J., Soares-Santos, M., Strauss, M. A., & et al. 2014, *The Astrophysical Journal*, 794, 120, doi: [10.1088/0004-637x/794/2/120](https://doi.org/10.1088/0004-637x/794/2/120)
- Applegate, D. E., von der Linden, A., Kelly, P. L., et al. 2014, *Monthly Notices of the Royal Astronomical Society*, 439, 48–72, doi: [10.1093/mnras/stt2129](https://doi.org/10.1093/mnras/stt2129)
- Astropy Collaboration, Robitaille, T. P., Tollerud, E. J., et al. 2013a, *aap*, 558, A33, doi: [10.1051/0004-6361/201322068](https://doi.org/10.1051/0004-6361/201322068)
- . 2013b, *A&A*, 558, A33, doi: [10.1051/0004-6361/201322068](https://doi.org/10.1051/0004-6361/201322068)
- Astropy Collaboration, Price-Whelan, A. M., Sipőcz, B. M., et al. 2018, *AJ*, 156, 123, doi: [10.3847/1538-3881/aabc4f](https://doi.org/10.3847/1538-3881/aabc4f)
- Astropy Collaboration, Price-Whelan, A. M., Lim, P. L., et al. 2022, *ApJ*, 935, 167, doi: [10.3847/1538-4357/ac7c74](https://doi.org/10.3847/1538-4357/ac7c74)
- Augusto, P., Edge, A. C., & Chandler, C. J. 2006, *Monthly Notices of the Royal Astronomical Society*, 367, 366–374, doi: [10.1111/j.1365-2966.2005.09965.x](https://doi.org/10.1111/j.1365-2966.2005.09965.x)
- Bacchi, M., Feretti, L., Giovannini, G., & Govoni, F. 2003, *A&A*, 400, 465, doi: [10.1051/0004-6361:20030044](https://doi.org/10.1051/0004-6361:20030044)
- Bergé, J., Price, S., Amara, A., & Rhodes, J. 2011, *Monthly Notices of the Royal Astronomical Society*, 419, 2356–2368, doi: [10.1111/j.1365-2966.2011.19888.x](https://doi.org/10.1111/j.1365-2966.2011.19888.x)
- Bernardeau, F., van Waerbeke, L., & Mellier, Y. 1997, *Weak Lensing Statistics as a Probe of Omega and Power Spectrum*. <https://arxiv.org/abs/astro-ph/9609122>
- Bernstein, G. M., & Jarvis, M. 2002, *The Astronomical Journal*, 123, 583, doi: [10.1086/338085](https://doi.org/10.1086/338085)
- Bertin, E., & Arnouts, S. 1996, *A&AS*, 117, 393, doi: [10.1051/aas:1996164](https://doi.org/10.1051/aas:1996164)

- Bertin, E., Mellier, Y., Radovich, M., et al. 2002, in *Astronomical Society of the Pacific Conference Series*, Vol. 281, *Astronomical Data Analysis Software and Systems XI*, ed. D. A. Bohlender, D. Durand, & T. H. Handley, 228
- Biava, N., Bonafede, A., Gastaldello, F., et al. 2024, First evidence of a connection between cluster-scale diffuse radio emission in cool-core galaxy clusters and sloshing features. <https://arxiv.org/abs/2403.09802>
- Bonafede, A., Intema, H. T., Brüggen, M., et al. 2014, *Monthly Notices of the Royal Astronomical Society: Letters*, 444, L44–L48, doi: [10.1093/mnras/lu110](https://doi.org/10.1093/mnras/lu110)
- Bond, J. R., Cole, S., Efstathiou, G., & Kaiser, N. 1991, *ApJ*, 379, 440, doi: [10.1086/170520](https://doi.org/10.1086/170520)
- Botteon, A., Shimwell, T. W., Cassano, R., et al. 2022, *A&A*, 660, A78, doi: [10.1051/0004-6361/202143020](https://doi.org/10.1051/0004-6361/202143020)
- Bradač, M., Lombardi, M., & Schneider, P. 2004, *Astronomy and Astrophysics*, 424, 13–22, doi: [10.1051/0004-6361:20035744](https://doi.org/10.1051/0004-6361:20035744)
- Brammer, G. B., van Dokkum, P. G., & Coppi, P. 2008, *The Astrophysical Journal*, 686, 1503–1513, doi: [10.1086/591786](https://doi.org/10.1086/591786)
- Brown, A. G. A., Vallenari, A., Prusti, T., et al. 2016, *Astronomy and Astrophysics*, 595, A2, doi: [10.1051/0004-6361/201629512](https://doi.org/10.1051/0004-6361/201629512)
- . 2021, *Astronomy & Astrophysics*, 650, C3, doi: [10.1051/0004-6361/202039657e](https://doi.org/10.1051/0004-6361/202039657e)
- Brunetti, G., & Jones, T. W. 2014, *International Journal of Modern Physics D*, 23, 1430007, doi: [10.1142/S0218271814300079](https://doi.org/10.1142/S0218271814300079)
- Burke, C. J., Peterson, J. R., Egami, E., et al. 2019, *Journal of Astronomical Telescopes, Instruments, and Systems*, 5, 1, doi: [10.1117/1.jatis.5.3.038002](https://doi.org/10.1117/1.jatis.5.3.038002)
- Carlstrom, J. E., Holder, G. P., & Reese, E. D. 2002, *ARA&A*, 40, 643, doi: [10.1146/annurev.astro.40.060401.093803](https://doi.org/10.1146/annurev.astro.40.060401.093803)
- Chambers, K. C., Magnier, E. A., Metcalfe, N., et al. 2016, *arXiv e-prints*, arXiv:1612.05560. <https://arxiv.org/abs/1612.05560>
- Chang, C., Marshall, P. J., Jernigan, J. G., et al. 2012, *Monthly Notices of the Royal Astronomical Society*, 427, 2572–2587, doi: [10.1111/j.1365-2966.2012.22134.x](https://doi.org/10.1111/j.1365-2966.2012.22134.x)
- Clowe, D., Bradač, M., Gonzalez, A. H., et al. 2006, *The Astrophysical Journal*, 648, L109–L113, doi: [10.1086/508162](https://doi.org/10.1086/508162)
- Cuciti, V., Cassano, R., Sereno, M., et al. 2023, *A&A*, 680, A30, doi: [10.1051/0004-6361/202346755](https://doi.org/10.1051/0004-6361/202346755)
- Cunha, C., Huterer, D., & Frieman, J. A. 2009, *Physical Review D*, 80, doi: [10.1103/physrevd.80.063532](https://doi.org/10.1103/physrevd.80.063532)
- Danese, L., de Zotti, G., & di Tullio, G. 1980, *A&A*, 82, 322
- Dawson, W. A., Schneider, M. D., Tyson, J. A., & Jee, M. J. 2015, *The Astrophysical Journal*, 816, 11, doi: [10.3847/0004-637x/816/1/11](https://doi.org/10.3847/0004-637x/816/1/11)
- Dietrich, J. P., Bocquet, S., Schrabback, T., et al. 2018, *Monthly Notices of the Royal Astronomical Society*, 483, 2871–2906, doi: [10.1093/mnras/sty3088](https://doi.org/10.1093/mnras/sty3088)
- Dutta, A., Peterson, J. R., & Sembroski, G. 2024, *Forced Measurement of Astronomical Sources at Low Signal to Noise*. <https://arxiv.org/abs/2405.12212>
- Edge, A. C., Ivison, R. J., Smail, I., Blain, A. W., & Kneib, J. P. 1999, *MNRAS*, 306, 599, doi: [10.1046/j.1365-8711.1999.02539.x](https://doi.org/10.1046/j.1365-8711.1999.02539.x)
- Ettori, S. 2000, *Monthly Notices of the Royal Astronomical Society*, 318, 1041, doi: [10.1046/j.1365-8711.2000.03664.x](https://doi.org/10.1046/j.1365-8711.2000.03664.x)
- Ettori, S., Donnarumma, A., Pointecouteau, E., et al. 2013, *Space Science Reviews*, 177, 119–154, doi: [10.1007/s11214-013-9976-7](https://doi.org/10.1007/s11214-013-9976-7)
- Evrard, A. E., Metzler, C. A., & Navarro, J. F. 1996, *ApJ*, 469, 494, doi: [10.1086/177798](https://doi.org/10.1086/177798)
- Fabian, A. C. 1994, *ARA&A*, 32, 277, doi: [10.1146/annurev.aa.32.090194.001425](https://doi.org/10.1146/annurev.aa.32.090194.001425)
- Fu, S., Dell’Antonio, I., Chary, R.-R., et al. 2022, *ApJ*, 933, 84, doi: [10.3847/1538-4357/ac68e8](https://doi.org/10.3847/1538-4357/ac68e8)
- Fukugita, M., Hogan, C. J., & Peebles, P. J. E. 1998, *The Astrophysical Journal*, 503, 518–530, doi: [10.1086/306025](https://doi.org/10.1086/306025)
- Gal, R. R., Lopes, P. A. A., de Carvalho, R. R., et al. 2009, *The Astronomical Journal*, 137, 2981–2999, doi: [10.1088/0004-6256/137/2/2981](https://doi.org/10.1088/0004-6256/137/2/2981)
- Gentile, M., Courbin, F., & Meylan, G. 2012, *Astronomy & Astrophysics*, 549, A1, doi: [10.1051/0004-6361/201219739](https://doi.org/10.1051/0004-6361/201219739)
- Giles, P. A., Romer, A. K., Wilkinson, R., et al. 2022, *Monthly Notices of the Royal Astronomical Society*, 516, 3878–3899, doi: [10.1093/mnras/stac2414](https://doi.org/10.1093/mnras/stac2414)
- Gitti, M., Brighenti, F., & McNamara, B. R. 2012, *Advances in Astronomy*, 2012, 1–24, doi: [10.1155/2012/950641](https://doi.org/10.1155/2012/950641)
- Gruen, D., Brimiouille, F., Seitz, S., et al. 2013, *Monthly Notices of the Royal Astronomical Society*, 432, 1455–1467, doi: [10.1093/mnras/stt566](https://doi.org/10.1093/mnras/stt566)
- Gunn, J. E., & Weinberg, D. H. 1994, *The Sloan Digital Sky Survey*. <https://arxiv.org/abs/astro-ph/9412080>
- Haines, C. P., Finoguenov, A., Smith, G. P., et al. 2018, *Monthly Notices of the Royal Astronomical Society*, 477, 4931–4950, doi: [10.1093/mnras/sty651](https://doi.org/10.1093/mnras/sty651)
- Harbeck, D. R., Boroson, T., Lesser, M., et al. 2014, in *Society of Photo-Optical Instrumentation Engineers (SPIE) Conference Series*, Vol. 9147, *Ground-based and Airborne Instrumentation for Astronomy V*, ed. S. K. Ramsay, I. S. McLean, & H. Takami, 91470P, doi: [10.1117/12.2056651](https://doi.org/10.1117/12.2056651)

- Harbeck, D. R., Lesser, M., Liu, W., et al. 2018, The WIYN One Degree Imager in 2018: An Extended 30-Detector Focal Plane. <https://arxiv.org/abs/1806.01913>
- Harris, C. R., Millman, K. J., van der Walt, S. J., et al. 2020, *Nature*, 585, 357, doi: [10.1038/s41586-020-2649-2](https://doi.org/10.1038/s41586-020-2649-2)
- Hartlap, J., Hilbert, S., Schneider, P., & Hildebrandt, H. 2011, *Astronomy & Astrophysics*, 528, A51, doi: [10.1051/0004-6361/201015850](https://doi.org/10.1051/0004-6361/201015850)
- Hirata, C. M., Yamamoto, M., Laliotis, K., et al. 2024, Simulating image coaddition with the Nancy Grace Roman Space Telescope: I. Simulation methodology and general results. <https://arxiv.org/abs/2303.08749>
- Hoekstra, H. 2004, *MNRAS*, 347, 1337, doi: [10.1111/j.1365-2966.2004.07327.x](https://doi.org/10.1111/j.1365-2966.2004.07327.x)
- Holder, G., Haiman, Z., & Mohr, J. J. 2001, *The Astrophysical Journal*, 560, L111–L114, doi: [10.1086/324309](https://doi.org/10.1086/324309)
- Hunter, J. D. 2007, *Computing in Science & Engineering*, 9, 90, doi: [10.1109/MCSE.2007.55](https://doi.org/10.1109/MCSE.2007.55)
- Hutchings, J. B., Saintonge, A., Schade, D., & Frenette, D. 2002, *The Astronomical Journal*, 123, 1826–1837, doi: [10.1086/339305](https://doi.org/10.1086/339305)
- HyeongHan, K., Jee, M. J., Cha, S., & Cho, H. 2023, Weak-Lensing Detection of Intracluster Filaments in the Coma Cluster. <https://arxiv.org/abs/2310.03073>
- Jain, B., & Seljak, U. 1997, *The Astrophysical Journal*, 484, 560–573, doi: [10.1086/304372](https://doi.org/10.1086/304372)
- Jauzac, M., Jullo, E., Kneib, J.-P., et al. 2012, *Monthly Notices of the Royal Astronomical Society*, 426, 3369–3384, doi: [10.1111/j.1365-2966.2012.21966.x](https://doi.org/10.1111/j.1365-2966.2012.21966.x)
- Jee, M. J., & Tyson, J. A. 2011, *Publications of the Astronomical Society of the Pacific*, 123, 596, doi: [10.1086/660137](https://doi.org/10.1086/660137)
- Kaiser, N. 1995, *ApJL*, 439, L1, doi: [10.1086/187730](https://doi.org/10.1086/187730)
- Kaiser, N., & Squires, G. 1993, *ApJ*, 404, 441, doi: [10.1086/172297](https://doi.org/10.1086/172297)
- Kaiser, N., Squires, G., & Broadhurst, T. 1995, *ApJ*, 449, 460, doi: [10.1086/176071](https://doi.org/10.1086/176071)
- Kaiser, N., Aussen, H., Burke, B., et al. 2002, *Proceedings of SPIE - The International Society for Optical Engineering*, 4836, 154, doi: [10.1117/12.457365](https://doi.org/10.1117/12.457365)
- Khatri, R. 2016, *Astronomy and Astrophysics*, 592, A48, doi: [10.1051/0004-6361/201526479](https://doi.org/10.1051/0004-6361/201526479)
- Kotulla, R. 2013, The QuickReduce data reduction pipeline for the WIYN One Degree Imager. <https://arxiv.org/abs/1310.5046>
- Krause, E., Pierpaoli, E., Dolag, K., & Borgani, S. 2011, *Monthly Notices of the Royal Astronomical Society*, 419, 1766–1779, doi: [10.1111/j.1365-2966.2011.19844.x](https://doi.org/10.1111/j.1365-2966.2011.19844.x)
- Kravtsov, A. V., & Borgani, S. 2012, *Annual Review of Astronomy and Astrophysics*, 50, 353–409, doi: [10.1146/annurev-astro-081811-125502](https://doi.org/10.1146/annurev-astro-081811-125502)
- Lacey, C., & Cole, S. 1993, *MNRAS*, 262, 627, doi: [10.1093/mnras/262.3.627](https://doi.org/10.1093/mnras/262.3.627)
- Lang, D., Hogg, D. W., & Schlegel, D. J. 2016, *aj*, 151, 36, doi: [10.3847/0004-6256/151/2/36](https://doi.org/10.3847/0004-6256/151/2/36)
- Lupton, R., Gunn, J. E., Ivezić, Z., Knapp, G. R., & Kent, S. 2001, in *Astronomical Society of the Pacific Conference Series*, Vol. 238, *Astronomical Data Analysis Software and Systems X*, ed. J. Harnden, F. R., F. A. Primini, & H. E. Payne, 269, doi: [10.48550/arXiv.astro-ph/0101420](https://doi.org/10.48550/arXiv.astro-ph/0101420)
- Mandelbaum, R. 2018, *Annual Review of Astronomy and Astrophysics*, 56, 393–433, doi: [10.1146/annurev-astro-081817-051928](https://doi.org/10.1146/annurev-astro-081817-051928)
- Mandelbaum, R., Rowe, B., Bosch, J., et al. 2014, *The Astrophysical Journal Supplement Series*, 212, 5, doi: [10.1088/0067-0049/212/1/5](https://doi.org/10.1088/0067-0049/212/1/5)
- Martino, R., Mazzotta, P., Bourdin, H., et al. 2014, *Monthly Notices of the Royal Astronomical Society*, 443, 2342–2360, doi: [10.1093/mnras/stu1267](https://doi.org/10.1093/mnras/stu1267)
- Massey, R., Rhodes, J., Leauthaud, A., et al. 2007, *The Astrophysical Journal Supplement Series*, 172, 239–253, doi: [10.1086/516599](https://doi.org/10.1086/516599)
- McCleary, J., dell’Antonio, I., & von der Linden, A. 2020, *The Astrophysical Journal*, 893, 8, doi: [10.3847/1538-4357/ab7c58](https://doi.org/10.3847/1538-4357/ab7c58)
- Miller, L., Heymans, C., Kitching, T. D., et al. 2013, *MNRAS*, 429, 2858, doi: [10.1093/mnras/sts454](https://doi.org/10.1093/mnras/sts454)
- Narasimha, D., & Chitre, S. M. 1993, *Journal of Astrophysics and Astronomy*, 14, 121, doi: [10.1007/BF02702361](https://doi.org/10.1007/BF02702361)
- Navarro, J. F., Frenk, C. S., & White, S. D. M. 1995, *MNRAS*, 275, 720, doi: [10.1093/mnras/275.3.720](https://doi.org/10.1093/mnras/275.3.720)
- Okabe, N., Takada, M., Umetsu, K., Futamase, T., & Smith, G. P. 2010, *PASJ*, 62, 811, doi: [10.1093/pasj/62.3.811](https://doi.org/10.1093/pasj/62.3.811)
- Peterson, J. R., Peng, E., Burke, C. J., Sembroski, G., & Cheng, J. 2019, *The Astrophysical Journal*, 873, 98, doi: [10.3847/1538-4357/ab0418](https://doi.org/10.3847/1538-4357/ab0418)
- Peterson, J. R., Sembroski, G., Dutta, A., & Remacaldo, C. 2024, Self-Consistent Atmosphere Representation and Interaction in Photon Monte Carlo Simulations. <https://arxiv.org/abs/2403.15562>
- Peterson, J. R., Jernigan, J. G., Kahn, S. M., et al. 2015, *The Astrophysical Journal Supplement Series*, 218, 14, doi: [10.1088/0067-0049/218/1/14](https://doi.org/10.1088/0067-0049/218/1/14)
- Peterson, J. R., O’Connor, P., Nomerotski, A., et al. 2020, *The Astrophysical Journal*, 889, 182, doi: [10.3847/1538-4357/ab64e0](https://doi.org/10.3847/1538-4357/ab64e0)

- Pierre, M., Le Borgne, J. F., Soucail, G., & Kneib, J. P. 1996, *A&A*, 311, 413, doi: [10.48550/arXiv.astro-ph/9510128](https://doi.org/10.48550/arXiv.astro-ph/9510128)
- Piffaretti, R., & Valdarnini, R. 2008, *Astronomy and Astrophysics*, 491, 71–87, doi: [10.1051/0004-6361:200809739](https://doi.org/10.1051/0004-6361:200809739)
- Postman, M., Coe, D., Benítez, N., et al. 2012, *ApJS*, 199, 25, doi: [10.1088/0067-0049/199/2/25](https://doi.org/10.1088/0067-0049/199/2/25)
- Press, W. H., & Schechter, P. 1974, *ApJ*, 187, 425, doi: [10.1086/152650](https://doi.org/10.1086/152650)
- Refregier, A. 2003, *Annual Review of Astronomy and Astrophysics*, 41, 645–668, doi: [10.1146/annurev.astro.41.111302.102207](https://doi.org/10.1146/annurev.astro.41.111302.102207)
- Reiprich, T. H., & Böhringer, H. 2002, *ApJ*, 567, 716, doi: [10.1086/338753](https://doi.org/10.1086/338753)
- Robitaille, T. 2019, *APLpy v2.0: The Astronomical Plotting Library in Python*, doi: [10.5281/zenodo.2567476](https://doi.org/10.5281/zenodo.2567476)
- Robitaille, T., & Bressert, E. 2012, *APLpy: Astronomical Plotting Library in Python*, *Astrophysics Source Code Library*. <http://ascl.net/1208.017>
- Rose, T., Edge, A. C., Combes, F., et al. 2019, *Monthly Notices of the Royal Astronomical Society*, 489, 349–365, doi: [10.1093/mnras/stz2138](https://doi.org/10.1093/mnras/stz2138)
- Rose, T., Edge, A., Kiehlmann, S., et al. 2022, *MNRAS*, 509, 2869, doi: [10.1093/mnras/stab3217](https://doi.org/10.1093/mnras/stab3217)
- Rose, T., McNamara, B. R., Combes, F., et al. 2024a, *Monthly Notices of the Royal Astronomical Society*, 528, 3441, doi: [10.1093/mnras/stae213](https://doi.org/10.1093/mnras/stae213)
- . 2024b, Two distinct molecular cloud populations detected in massive galaxies. <https://arxiv.org/abs/2403.03974>
- Rozo, E., Rykoff, E. S., Becker, M., Reddick, R. M., & Wechsler, R. H. 2015, *Monthly Notices of the Royal Astronomical Society*, 453, 38–52, doi: [10.1093/mnras/stv1560](https://doi.org/10.1093/mnras/stv1560)
- Savini, F., Bonafede, A., Brüggén, M., et al. 2019, *Astronomy and Astrophysics*, 622, A24, doi: [10.1051/0004-6361/201833882](https://doi.org/10.1051/0004-6361/201833882)
- Schirmer, M., Erben, T., Schneider, P., Wolf, C., & Meisenheimer, K. 2004, *Astronomy and Astrophysics*, 420, 75–78, doi: [10.1051/0004-6361:20041072](https://doi.org/10.1051/0004-6361:20041072)
- Schneider, P. 1996, *Monthly Notices of the Royal Astronomical Society*, 283, 837–853, doi: [10.1093/mnras/283.3.837](https://doi.org/10.1093/mnras/283.3.837)
- Seitz, C., & Schneider, P. 1995, *A&A*, 297, 287, doi: [10.48550/arXiv.astro-ph/9408050](https://doi.org/10.48550/arXiv.astro-ph/9408050)
- Smith, S. 1936, *ApJ*, 83, 23, doi: [10.1086/143697](https://doi.org/10.1086/143697)
- Sommer, M. W., Basu, K., Intema, H., et al. 2016, *Monthly Notices of the Royal Astronomical Society*, 466, 996–1009, doi: [10.1093/mnras/stw3015](https://doi.org/10.1093/mnras/stw3015)
- Sonkamble, S. S., Vagshette, N. D., Pawar, P. K., & Patil, M. K. 2015, *Astrophysics and Space Science*, 359, doi: [10.1007/s10509-015-2508-z](https://doi.org/10.1007/s10509-015-2508-z)
- Squires, G., Kaiser, N., Fahlman, G., Babul, A., & Woods, D. 1996, *ApJ*, 469, 73, doi: [10.1086/177759](https://doi.org/10.1086/177759)
- Stoughton, C., Lupton, R. H., Bernardi, M., et al. 2002, *AJ*, 123, 485, doi: [10.1086/324741](https://doi.org/10.1086/324741)
- Sunyaev, R. A., & Zeldovich, I. B. 1980, *ARA&A*, 18, 537, doi: [10.1146/annurev.aa.18.090180.002541](https://doi.org/10.1146/annurev.aa.18.090180.002541)
- Sunyaev, R. A., & Zeldovich, Y. B. 1970, *Ap&SS*, 7, 3, doi: [10.1007/BF00653471](https://doi.org/10.1007/BF00653471)
- . 1972, *Comments on Astrophysics and Space Physics*, 4, 173
- The Dark Energy Survey Collaboration. 2005, *arXiv e-prints*, astro, doi: [10.48550/arXiv.astro-ph/0510346](https://doi.org/10.48550/arXiv.astro-ph/0510346)
- Tyson, J. A., Roat, C., Bosch, J., & Wittman, D. 2008, *LSST and the Dark Sector: Image Processing Challenges*. <https://arxiv.org/abs/0808.3425>
- Tyson, J. A., Valdes, F., & Wenk, R. A. 1990, *ApJL*, 349, L1, doi: [10.1086/185636](https://doi.org/10.1086/185636)
- Umetsu, K., Birkinshaw, M., Liu, G.-C., et al. 2009, *The Astrophysical Journal*, 694, 1643–1663, doi: [10.1088/0004-637x/694/2/1643](https://doi.org/10.1088/0004-637x/694/2/1643)
- van Haarlem, M., & van de Weygaert, R. 1993, *ApJ*, 418, 544, doi: [10.1086/173416](https://doi.org/10.1086/173416)
- Van Waerbeke, L., Mellier, Y., Pelló, R., et al. 2002, *Astronomy & Astrophysics*, 393, 369–379, doi: [10.1051/0004-6361:20020932](https://doi.org/10.1051/0004-6361:20020932)
- van Weeren, R. J., de Gasperin, F., Akamatsu, H., et al. 2019, *Space Science Reviews*, 215, doi: [10.1007/s11214-019-0584-z](https://doi.org/10.1007/s11214-019-0584-z)
- Venturi, T., Rossetti, M., Brunetti, G., et al. 2017, *Astronomy and Astrophysics*, 603, A125, doi: [10.1051/0004-6361/201630014](https://doi.org/10.1051/0004-6361/201630014)
- Virtanen, P., Gommers, R., Oliphant, T. E., et al. 2020, *Nature Methods*, 17, 261, doi: [10.1038/s41592-019-0686-2](https://doi.org/10.1038/s41592-019-0686-2)
- von der Linden, A., Allen, M. T., Applegate, D. E., et al. 2014, *Monthly Notices of the Royal Astronomical Society*, 439, 2–27, doi: [10.1093/mnras/stt1945](https://doi.org/10.1093/mnras/stt1945)
- Wen, Z. L., & Han, J. L. 2015, *The Astrophysical Journal*, 807, 178, doi: [10.1088/0004-637x/807/2/178](https://doi.org/10.1088/0004-637x/807/2/178)
- Wen, Z. L., Han, J. L., & Liu, F. S. 2012, *The Astrophysical Journal Supplement Series*, 199, 34, doi: [10.1088/0067-0049/199/2/34](https://doi.org/10.1088/0067-0049/199/2/34)
- Zackay, B., & Ofek, E. O. 2017, *The Astrophysical Journal*, 836, 187, doi: [10.3847/1538-4357/836/2/187](https://doi.org/10.3847/1538-4357/836/2/187)
- Zuntz, J., Sheldon, E., Samuroff, S., et al. 2018, *Monthly Notices of the Royal Astronomical Society*, 481, 1149–1182, doi: [10.1093/mnras/sty2219](https://doi.org/10.1093/mnras/sty2219)
- Zwicky, F. 1933, *Helvetica Physica Acta*, 6, 110

—. 1937, *ApJ*, 86, 217, doi: [10.1086/143864](https://doi.org/10.1086/143864)